A Hard X-Ray Power-Law Spectral Cutoff in Centaurus X-4

Chakrabarty, Deepto; Tomsick, John A.; Grefenstette, Brian W.; Psaltis, Dimitrios; Bachetti, Matteo; Barret, Didier; Boggs, Steven E.; Christensen, Finn Erland; Craig, William W.; Fuerst, Felix; Hailey, Charles J.; Harrison, Fiona A.; Kaspi, Victoria A.; Miller, Jon M.; Nowak, Michael A.; Rana, Vikram; Stern, Daniel; Wik, Daniel R.; Wilms, Joern; Zhang, William W.

Published in:
Astrophysical Journal

Link to article, DOI:
10.1088/0004-637X/797/2/92

Publication date:
2015

Document Version
Publisher's PDF, also known as Version of record

The Astrophysical Journal, 797:92 (15pp), 2014 December 20 doi:10.1088/0004-637X/797/2/92

A HARD X-RAY POWER-LAW SPECTRAL CUTOFF IN CENTAURUS X-4

Deepto Chakrabarty[1], John A. Tomsick[2], Brian W. Grefenstette[3], Dimitrios Psaltis[4], Matteo Bachetti[5,6], Didier Barret[5,6], Steven E. Boggs[2], Finn E. Christensen[7], William W. Craig[2,8], Felix Fürst[3], Charles J. Hailey[9], Fiona A. Harrison[3], Victoria M. Kaspi[10], Jon M. Miller[11], Michael A. Nowak[1], Vikram Rana[3], Daniel Stern[12], Daniel R. Wik[13], Jörn Wilms[14], and William W. Zhang[13]
[1] MIT Kavli Institute for Astrophysics and Space Research, Massachusetts Institute of Technology, Cambridge, MA 02139, USA; deepto@mit.edu
[2] Space Sciences Laboratory, University of California, Berkeley, CA 94720, USA
[3] Cahill Center for Astronomy and Astrophysics, California Institute of Technology, Pasadena, CA 91125, USA
[4] Department of Astronomy, University of Arizona, Tucson, AZ 85721, USA
[5] Observatoire Midi-Pyrénées, Université de Toulouse III – Paul Sabatier, F-31400 Toulouse, France
[6] CNRS, Institut de Recherche en Astrophysique et Planetologie, F-31028 Toulouse, France
[7] Division of Astrophysics, National Space Institute, Technical University of Denmark, DK-2800 Lyngby, Denmark
[8] Lawrence Livermore National Laboratory, Livermore, CA 94550, USA
[9] Columbia Astrophysics Laboratory, Columbia University, New York, NY 10027, USA
[10] Department of Physics, McGill University, Montreal, PQ H3A 2T8, Canada
[11] Department of Astronomy, University of Michigan, Ann Arbor, MI 48109, USA
[12] Jet Propulsion Laboratory, California Institute of Technology, Pasadena, CA 91109, USA
[13] Astrophysics Science Division, NASA Goddard Space Flight Center, Greenbelt, MD 20771, USA
[14] Dr. Karl-Remeis-Sternwarte and Erlangen Centre for Astroparticle Physics, Universität Erlangen-Nürnberg, D-96049 Bamberg, Germany
Received 2014 March 26; accepted 2014 October 8; published 2014 December 3

ABSTRACT

The low-mass X-ray binary (LMXB) Cen X-4 is the brightest and closest (<1.2 kpc) quiescent neutron star transient. Previous 0.5–10 keV X-ray observations of Cen X-4 in quiescence identified two spectral components: soft thermal emission from the neutron star atmosphere and a hard power-law tail of unknown origin. We report here on a simultaneous observation of Cen X-4 with *NuSTAR* (3–79 keV) and *XMM-Newton* (0.3–10 keV) in 2013 January, providing the first sensitive hard X-ray spectrum of a quiescent neutron star transient. The 0.3–79 keV luminosity was $1.1 \times 10^{33}\ D_{\rm kpc}^2$ erg s^{-1}, with $\simeq$60% in the thermal component. We clearly detect a cutoff of the hard spectral tail above 10 keV, the first time such a feature has been detected in this source class. We show that thermal Comptonization and synchrotron shock origins for the hard X-ray emission are ruled out on physical grounds. However, the hard X-ray spectrum is well fit by a thermal bremsstrahlung model with $kT_e = 18$ keV, which can be understood as arising either in a hot layer above the neutron star atmosphere or in a radiatively inefficient accretion flow. The power-law cutoff energy may be set by the degree of Compton cooling of the bremsstrahlung electrons by thermal seed photons from the neutron star surface. Lower thermal luminosities should lead to higher (possibly undetectable) cutoff energies. We compare Cen X-4's behavior with PSR J1023+0038, IGR J18245−2452, and XSS J12270−4859, which have shown transitions between LMXB and radio pulsar modes at a similar X-ray luminosity.

Key words: accretion, accretion disks – binaries: close – stars: individual (Cen X-4) – stars: neutron – X-rays: binaries

Online-only material: color figures

1. INTRODUCTION

Low-mass X-ray binaries (LMXBs) consist of a neutron star (NS) or black hole (BH) accreting from a low-mass ($\lesssim 1\ M_\odot$) stellar companion via Roche-lobe overflow. They may be divided into two categories: persistent accretors with X-ray luminosity $L_{\rm x} \gtrsim 10^{36}$ erg s^{-1} and transient systems. Transient LMXBs undergo recurrent bright ($L_{\rm x} \gtrsim 10^{36}$ erg s^{-1}) outbursts lasting days to weeks and then return to long intervals of X-ray quiescence ($L_{\rm x} \lesssim 10^{34}$ erg s^{-1}) lasting months to years. The long-term average mass accretion rate of the transients is thus substantially lower than in the persistent systems, owing to their low duty cycle. Transient behavior is understood to arise from a thermal instability in the outer accretion disk wherein the viscosity (and thus the mass accretion rate $\dot{M}$ through the disk) jumps to a higher value when a critical surface density is reached as the disk fills up (see Lasota 2001, and references therein). The persistent LMXBs avoid this instability because their higher accretion rates lead to increased X-ray heating, keeping the disks permanently ionized (van Paradijs 1996; King et al. 1996).

For the NS systems, the 0.5–10 keV X-ray spectrum of quiescent LMXB transients typically consists of two components: a low-energy ("soft") ~0.1 keV thermal component, and a high-energy ("hard") power-law component with photon index $1 < \Gamma < 2$, where the photon flux $dN/dE \propto E^{-\Gamma}$. The soft component is generally well fit by a hydrogen atmosphere model for the NS. The leading explanation for the energy source of the soft component is a deep crustal heating model (Brown et al. 1998) in which the emission is powered by heat injected into the NS crust by pycnonuclear reactions driven by accretion during transient outbursts. In this model, the contribution of quiescent accretion is negligible. X-ray spectroscopy of soft thermal emission in quiescent NS transients has been used to infer NS radii (Brown et al. 1998; Rutledge et al. 1999; Guillot et al. 2013) and to study the thermal relaxation of NS crusts (see Wijnands et al. 2013, and references therein). However, a possible problem for such studies is that accretion may not have completely shut

off during quiescence, as suggested by the detection of quiescent variability in the two brightest quiescent NS/LMXBs, Aql X-1 (Rutledge et al. 2002) and Cen X-4 (Campana et al. 2004b; Bernardini et al. 2013). There has been considerable debate as to whether this variability is primarily in the soft thermal component, the hard power-law component, or both (e.g., Rutledge et al. 2002; Campana & Stella 2003; Cackett et al. 2005).

The origin of the hard power-law tail is unclear. It is not predicted by the deep crustal heating model (Brown et al. 1998). Two explanations have been discussed: synchrotron shock emission from a radio pulsar wind and Comptonization of the soft thermal photons by a hot corona (Campana et al. 1998a). The synchrotron model is of particular interest given the recent confirmation that NS/LMXBs can turn on as radio pulsars at low accretion rates (Archibald et al. 2009; Papitto et al. 2013). A difficulty in discriminating between the different models has been the absence of knowledge about how high the power-law component extends in energy, owing to a lack of sufficient observational sensitivity above 10 keV. The recent launch of the *NuSTAR* hard X-ray telescope provides the first opportunity to explore this question.

The ideal target with which to address this is Cen X-4, also known as X1455−314 (Galactic coordinates $l = 332.^{\circ}2$, $b = 23.^{\circ}9$), the brightest quiescent NS/LMXB. It was discovered in 1969 in the 3–12 keV band with the *Vela 5A/5B* satellites during an extremely bright (∼20 Crab at peak) X-ray outburst lasting over two months (Conner et al. 1969; Evans et al. 1970). A second bright (∼4 Crab at peak) X-ray outburst was detected in 1979 (Kaluzienski et al. 1980) along with counterparts in the optical (Canizares et al. 1980) and radio (Hjellming 1979; Hjellming et al. 1988), but the source has been in X-ray quiescence (∼$10^5\times$ fainter) ever since.

Bright X-ray flashes, now understood as thermonuclear (type I) X-ray bursts, were observed around the time of both the 1969 and 1979 outbursts (Belian et al. 1972; Matsuoka et al. 1980), conclusively establishing the source as an NS and setting an upper limit on the distance of 1.2 ± 0.3 kpc (Chevalier et al. 1989). A third burst may have been observed by the *Apollo 15* lunar mission in 1971 (Kuulkers et al. 2009). The presence of thermonuclear bursts indicates that the surface dipole magnetic field is weak, with $B_{\rm surf} \lesssim 10^{10}$ G (Joss & Li 1980) and most likely $\sim 10^8$ G (by analogy with other type I bursters). Optical photometry and spectroscopy indicate that the binary companion V822 Cen is a K3-7 V dwarf, the binary period is 15.1 hr, and the binary mass ratio is $q = 0.1755$ (Chevalier et al. 1989; Torres et al. 2002; D'Avanzo et al. 2005; Shahbaz et al. 2014). The best-fit NS mass is $1.94^{+0.37}_{-0.85}\ M_{\odot}$ (Shahbaz et al. 2014). Given the proximity and high Galactic latitude of the source, it has extremely low interstellar extinction and absorption, allowing more sensitive observations in the ultraviolet and soft X-ray bands than usually possible for LMXBs (Blair et al. 1984; McClintock & Remillard 2000; Park & Garcia 2011; Cackett et al. 2013). The integrated values along this line of sight are $A_V = 0.362$ (Schlafly & Finkbeiner 2011) and $N_{\rm H} \approx 9 \times 10^{20}$ cm^{-2} (Dickey & Lockman 1990; Kalberla et al. 2005).

Cen X-4 has been observed extensively during X-ray quiescence since the 1979 outburst, with deep X-ray spectra in the 0.5–10 keV range previously obtained on six occasions since 1994 (see Cackett et al. 2010, and references therein; see also Section 5.2). A long-term daily monitoring campaign with *Swift* recently demonstrated that the thermal and power-law components vary together on timescales from days to months, with no spectral change observed and each component contributing roughly half of the flux (Bernardini et al. 2013). These authors concluded that the quiescent X-ray emission in Cen X-4 is primarily generated by accretion.

In this paper, we present the first sensitive hard X-ray observation of Cen X-4 in quiescence with *NuSTAR*, obtained simultaneously with a deep *XMM-Newton* soft X-ray observation. We describe the observations in Section 2 and our spectral analysis and results in Section 3. We interpret our results in Section 4 and discuss their implications in Section 5.

2. OBSERVATIONS

2.1. NuSTAR

NuSTAR, the first focusing hard X-ray observatory in orbit, was launched in 2012 and operates in the 3–79 keV range (Harrison et al. 2013). It consists of two coaligned telescopes, and the two focal planes (FPMA and FPMB) are each covered by a 2×2 array of cadmium-zinc-telluride (CZT) pixel detectors. Our *NuSTAR* observation of Cen X-4 (ObsID 30001004002) began on 2013 January 20, 20:20 UT and had an elapsed duration of 219 ks, with an on-source exposure time of 114 ks. The source was imaged on detector 0 in both FPMA and FPMB. The data were processed and screened using the standard pipeline for on-axis point sources in the *NuSTAR* Data Analysis System (`nustardas`) version 1.2.0, along with the *NuSTAR* calibration database (CALDB) version 20130509. Light curves and spectra from both FPMA and FPMB were extracted from a circular region centered on the source position with a radius of 75 arcsec.

A detailed background model for the source position in each of the two telescopes was derived by using the `nuskybgd` tool (Wik et al. 2014) to fit blank sky regions covering the entire field of view for each focal plane. For faint point sources like Cen X-4, this is more accurate than the usual method of simply scaling from the background of a nearby blank sky region because it correctly accounts for the highly nonuniform background gradients across the detectors. In both telescopes, the background was brighter than the source above around 20 keV. The background-subtracted count rates in FPMA and FPMB were $(4.51 \pm 0.09) \times 10^{-2}$ count s^{-1} and $(4.08 \pm 0.09) \times 10^{-2}$ count s^{-1}, respectively. The *NuSTAR* spectra were rebinned so that all but the highest energy bin had a background-subtracted significance of at least 10σ. The highest energy bin had 5.2σ significance in FPMA (20–79 keV) and 4.3σ significance in FPMB (17–79 keV), demonstrating that the source was detected beyond 20 keV.

2.2. XMM-Newton

The *XMM-Newton* observatory, launched in 1999, is a focusing X-ray telescope operating in the 0.3–12 keV range (Jansen et al. 2001). Our *XMM-Newton* observation of Cen X-4 (ObsID 0692790201) began on 2013 January 21, 13:01 UT and had a duration of 35 ks; this was simultaneous with part of our *NuSTAR* observation. We used the data from all three coaligned imaging X-ray cameras (EPIC-pn, EPIC-MOS1, and EPIC-MOS2; Strüder et al. 2001; Turner et al. 2001). The cameras were operated in full-frame mode with the thin optical-blocking filter in place, resulting in a time resolution of 73 ms for EPIC-pn and 2.6 s for the MOS cameras. The data were reduced using the *XMM-Newton* Scientific Analysis System (SAS) v13.0.1, along with the latest calibration files available as of 2013 July 13. We reprocessed the data using `epproc` and `emproc` to produce new event files and applied standard event filtering. We identified

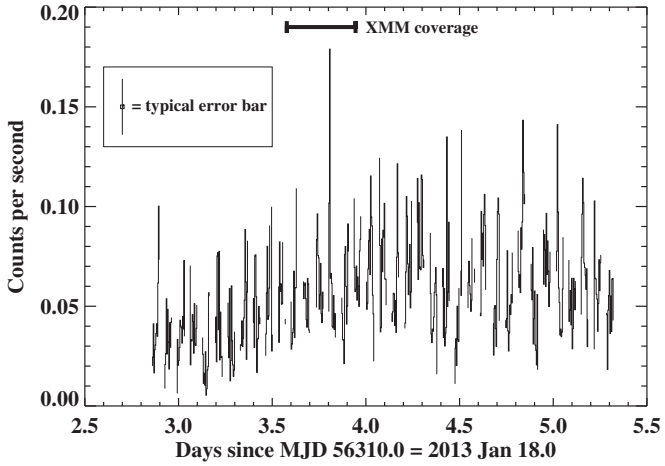

Figure 1. Background-subtracted 3–20 keV light curve of Cen X-4 measured with *NuSTAR*, binned at 300 s resolution. The average of the FPMA and FPMB count rates is plotted, and the size of a typical error bar is shown. The data gaps are due to Earth occultations. The source intensity varies significantly on timescales of minutes to hours. The interval with simultaneous coverage with *XMM-Newton* is indicated and includes a bright flare around MJD 56313.8 (see Figure 2).

background flare intervals by constructing a light curve of the 10–12 keV EPIC-pn data using events from the entire field of view and searching for intervals where the count rate exceeded 1 count s^{-1}. We found three short flares; these intervals were removed from our Cen X-4 event lists. The net exposure time was 27 ks for EPIC-pn and 30 ks for each of the EPIC-MOS units.

For all three detectors, we initially extracted light curves and spectra from a circular region centered on the source position with a radius of 43.5 arcsec. For the MOS detectors, we measured the background using a square blank-sky region 3×3 arcmin in size. For the EPIC-pn detector, an important consideration is that the outer parts of the field of view include photons that are due to Cu fluorescence in the instrument while the inner parts do not. Because Cen X-4 was in the region without the Cu emission line, we chose a rectangular region near Cen X-4 for determining the EPIC-pn background. The background-subtracted count rates in the 0.3–10 keV range were 2.58 ± 0.01 count s^{-1} in EPIC-pn, 0.640 ± 0.005 count s^{-1} in EPIC-MOS1, and 0.619 ± 0.005 count s^{-1} in EPIC-MOS2.

These count rates are higher than those observed in previous *XMM-Newton* observations (Cackett et al. 2010). In fact, the count rates in both the EPIC-MOS and EPIC-pn detectors are close to the threshold where photon pileup effects may begin to distort the measured spectra, particularly during the flares.[15] Moreover, our preliminary analysis found that the two EPIC-MOS spectra each have significant systematic differences with the EPIC-pn spectrum above 2 keV. As a precaution, we reextracted both the MOS and pn data from an annular region centered on the source position with an outer radius of 43.5 arcsec and an inner radius of 10 arcsec, thus excluding the core of the point-spread function (PSF) where any pileup would occur (at the expense of reduced counting statistics). The MOS and pn spectra from the annular region are mutually consistent. This annulus-only data set still includes sufficient counts to obtain a good measurement of the soft X-ray spectrum.

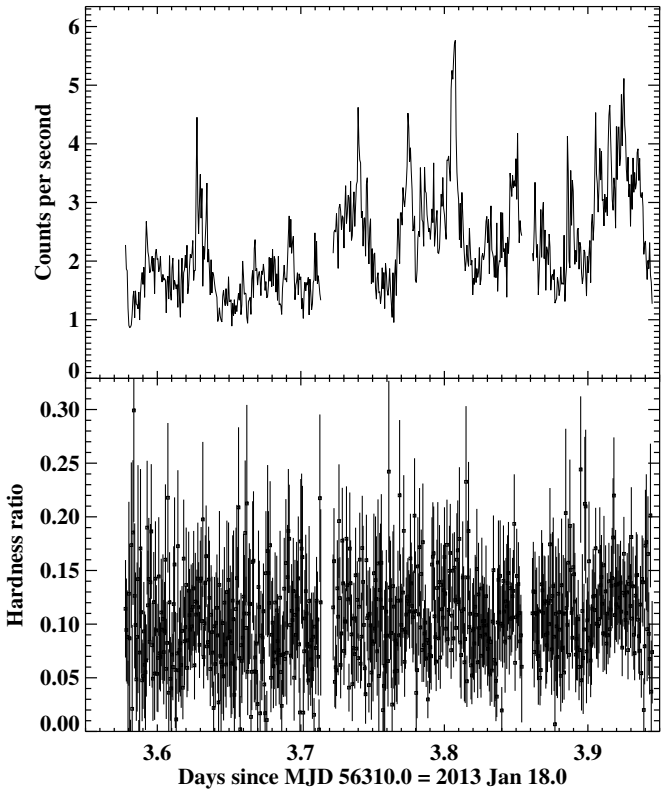

Figure 2. Top panel: background-subtracted 0.3–10 keV light curve of Cen X-4 measured with *XMM-Newton*/EPIC-pn, binned at 50 s resolution. The typical error bar is ± 0.16 counts s^{-1}. The short data gaps are intervals that were excluded owing to strong background flares. The source intensity shows strong flaring behavior, varying by more than a factor of two on timescales as short as a few minutes. The brightest flare, around MJD 56313.8, is also visible in the *NuSTAR* light curve (see Figure 1). Bottom panel: spectral hardness of the count rate shown in the top panel, constructed by taking the ratio of the 2–10 keV and 0.3–1.0 keV count rates. There is no evidence for significant spectral changes during the flaring intervals, although there is weak evidence for a small change during the flare at MJD 56313.63.

3. DATA ANALYSIS AND RESULTS

3.1. Timing

The light curves for the *NuSTAR* and *XMM-Newton* observations are shown in Figure 1 and the top panel of Figure 2, respectively. (The *XMM-Newton* light curve uses the full data set, not the annulus-only data.) Both light curves vary significantly on timescales of a few minutes. The *XMM-Newton* light curve clearly exhibits flaring activity; the strongest of these flares, around MJD 56313.8, is also easily visible in the *NuSTAR* light curve. The fractional excess rms variability[16] $F_{\rm var}$ was $37\% \pm 6\%$ in the *NuSTAR* light curve and $37\% \pm 2\%$ in the *XMM-Newton*/EPIC-pn light curve. For comparison, a value of $73.0\% \pm 1.5\%$ was measured in 60 short *Swift* observations made over three months (Bernardini et al. 2013).

A comparison of the 0.3–1 keV and 2–10 keV *XMM-Newton*/EPIC-pn light curves shows no evidence for significant spectral changes during these flares, although there is weak evidence for a small change during the flare at MJD 56313.63 (Figure 2, bottom panel; Figure 3). A cross-correlation analysis indicates that the flares in these two bands are simultaneous to within $\lesssim$30 s. We searched the *NuSTAR* light curve for evidence of

[15] See Table 3 in Section 3.3.2 of the *XMM-Newton Users Handbook*, v2.11, 2013, http://heasarc.gsfc.nasa.gov/docs/xmm/uhb/.

[16] This is a measure of the intrinsic source variability in excess of Poisson counting noise; see, e.g., Vaughan et al. (2003).

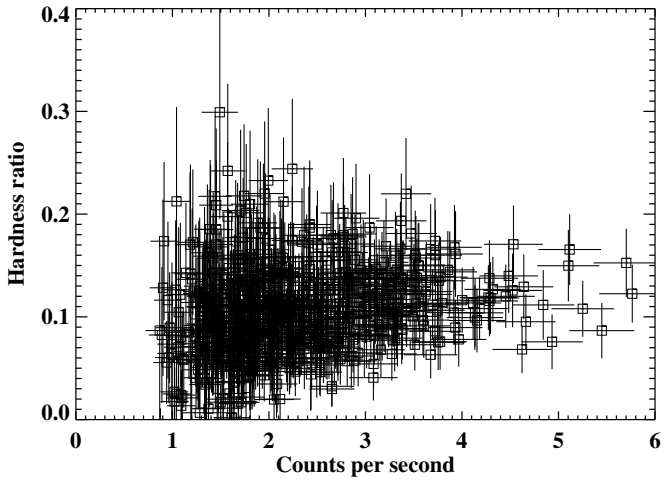

Figure 3. Hardness–intensity diagram for *XMM-Newton*/EPIC-pn observation of Cen X-4. The *x* axis shows the 0.3–10 keV count rate, and the *y* axis shows the spectral hardness (defined as the ratio of the 2–10 keV and 0.3–1.0 keV count rates). There is no evidence for significant spectral changes as a function of source intensity.

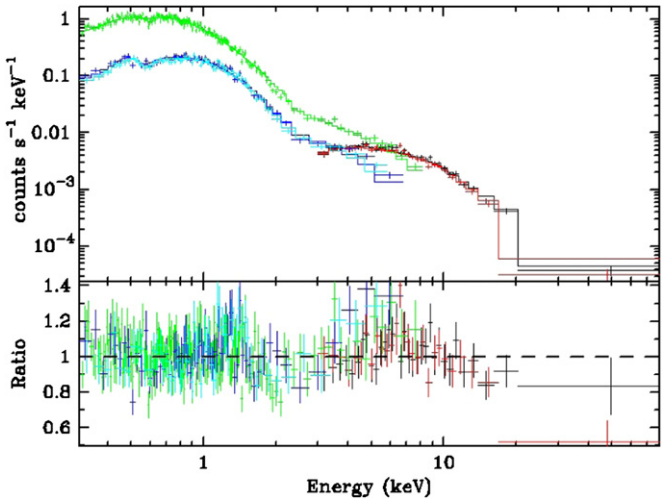

Figure 4. Count spectrum and fit for our joint *XMM-Newton* and *NuSTAR* observation of Cen X-4, using an unbroken power law to model the hard X-ray spectrum. The model used is `tbabs*(nsatmos+powerlaw)`. The *XMM-Newton* data were extracted from an annulus in order to avoid possible photon pileup effects (see Section 2.2). The green points are the *XMM-Newton* EPIC-pn data; the dark and light blue points are the *XMM-Newton* EPIC MOS1 and MOS2 data, respectively; and the black and red points are the *NuSTAR* FPMA and FPMB data, respectively. The residuals are consistent with a break in the power-law spectrum around 7 keV or a cutoff in the 10–20 keV range.

(A color version of this figure is available in the online journal.)

orbital variability by folding at the 15.1 hr binary period (Shahbaz et al. 2014). No orbital modulation was detected.

3.2. Spectroscopy

Because there is no evidence for significant spectral variability during the flares (Figure 2, bottom panel; Figure 3), we chose to include the flare intervals for our spectral analysis. We performed joint spectral fits of the *NuSTAR* and *XMM-Newton* (annulus) data with XSPEC version 12.8 spectral fitting software (Arnaud 1996) using χ^2-minimization. To allow for systematic calibration differences between the different detectors, we included a constant multiplicative factor in the model. This constant was set to unity for *XMM-Newton*/EPIC-pn but allowed to vary for the other detectors. All other spectral model parameters were tied together across the three instruments. Interstellar absorption was modeled using the `tbabs` model (Wilms et al. 2000) along with photoionization cross sections from Verner et al. (1996).

We tried two different models for the soft thermal component. We first fit a passively cooling NS atmosphere using the `nsatmos` model (Heinke et al. 2006), which assumes a pure H atmosphere and a negligible surface magnetic field ($B \lesssim 10^8$ G) and also includes the effects of surface gravity, heat conduction by electrons, and self-irradiation. In applying `nsatmos`, we fixed the source distance at 1.2 kpc (Chevalier et al. 1989) and assumed that the atmospheric emission was coming from the entire NS surface. We found that it was not possible to constrain the NS mass M and radius R when both were allowed to vary because a wide range of M-R pairs gave acceptable fits. We therefore fixed the NS mass to $M = 1.9\ M_\odot$ (Shahbaz et al. 2014). As an alternative model, we also tried fitting to the synthetic spectra of Zampieri et al. (1995, 2001) for thermal emission from unmagnetized NSs with a pure H atmosphere in the presence of very low accretion rates. These spectra have been implemented as the XSPEC additive table model `zamp` and are parameterized in terms of the observed accretion luminosity scaled to the Eddington rate (L_∞/L_E), with fixed NS mass $M = 1.4\ M_\odot$ and true radius $R = 12.4$ km. In practice, the model shapes from `nsatmos` and `zamp` are essentially identical (see, e.g., Soria et al. 2011), but it is useful to demonstrate that models that explicitly include accretion are consistent with the data.

Although previous 0.5–10 keV X-ray observations of Cen X-4 in quiescence were all well fit by an absorbed passive NS atmosphere plus power-law model (see Cackett et al. 2010, and references therein), the `tbabs*(nsatmos+powerlaw)` model does not provide a satisfactory fit to the high-energy data in our combined *NuSTAR*+*XMM-Newton* data covering the 0.3–79 keV range. The residuals indicate the presence of a spectral break or cutoff in the 10–20 keV range (see Figure 4). We found several different models that provided a good fit for the hard component: a cutoff power law (`cutoffpl`), a broken power law (`bknpower`), thermal Comptonization (`comptt`; Titarchuk 1994; Hua & Titarchuk 1995), and thermal bremsstrahlung (`bremss`). In each case, this component was combined with `tbabs` and either `nsatmos` or `zamp`. In all cases, the $N_{\rm H}$ value is consistent with the integrated interstellar value along the line of sight (Dickey & Lockman 1990; Kalberla et al. 2005). We found no evidence for fluorescent Fe line emission in the spectrum. The upper limit on the equivalent width of a narrow Gaussian Fe emission line at 6.4 keV is <120 eV (90%-confidence).

The spectral fits with `nsatmos` are summarized in Table 1; those with `zamp` are summarized in Table 2. A typical fit is shown in Figure 5. The corresponding unfolded spectrum is shown in Figure 6. We are able to obtain reasonably good fits with a wide variety of models. We note that the only spectral shape parameter in the `zamp` model is the accretion luminosity L_∞ observed at infinity; one must compare this with the measured flux and source distance to check for self-consistency. We find that the best-fit values of L_∞ are roughly consistent with the measured soft flux for the assumed distance of 1.2 kpc.

Using the `tbabs*(nsatmos+bremss)` model, we find an average (absorbed) flux of 3.8×10^{-12} erg cm^{-2} s^{-1} in the soft (0.3–3 keV) band and 3.3×10^{-12} erg cm^{-2} s^{-1} in the hard (3–79 keV) band. The unabsorbed soft luminosity was

Table 1
Spectral Fits with a Passive Neutron Star Atmosphere[a]

Parameter	Symbol	Units	Hard Spectral Component				
			`cutoffpl`	`bknpow`	`comptt(disk)`	`comptt(sphere)`	`bremss`
Absorption and `nsatmos` parameters							
Absorption column	$N_{\rm H}$	10^{21} cm^{-2}	0.88(4)	0.89(3)	0.92(4)	0.92(4)	0.87(5)
Temperature (unredshifted)	$\log T$	K	6.16(4)	6.18(1)	6.20(27)	6.19(23)	6.20(10)
Mass (fixed)	M	$M_\odot$	1.9	1.9	1.9	1.9	1.9
Radius	R	km	9.2(1.0)	8.6(2.6)	8.5(5.7)	8.6(4.9)	8.1(1.8)
Covering fraction (fixed)	$K_{\rm NS}$	···	1	1	1	1	1
Distance (fixed)	D	kpc	1.2	1.2	1.2	1.2	1.2
Hard spectral component parameters							
Normalization	K	10^{-4}	2.3(2)[b]	2.2(2)[b]	0.7(1)[b]	0.7(1)[b]	4.1(1)[c]
Photon index	Γ	···	1.02(10)	1.26(10)	···	···	···
Cutoff or break energy	E_c, E_b	keV	10.4(1.4)	5.8(3)	···	···	···
Photon index 2	Γ_2	···	···	2.02(5)	···	···	···
Electron temperature	kT_e	keV	···	···	6.4(1.1)	6.4(1.1)	18.2(1.0)
Seed temperature	kT_0	keV	···	···	0.74(8)	0.74(7)	···
Scattering optical depth	$\tau_{\rm es}$	···	···	···	4.0(5)	8.8(1.0)	···
Instrument multiplicative constants							
NuSTAR/FPMA	$C_{\rm FPMA}$	···	1.04(3)	1.03(3)	1.02(3)	1.02(3)	1.09(3)
NuSTAR/FPMB	$C_{\rm FPMB}$	···	1.07(4)	1.05(4)	1.05(4)	1.05(4)	1.12(4)
XMM/EPIC-pn (fixed)	$C_{\rm pn}$	···	1	1	1	1	1
XMM/EPIC-MOS1	$C_{\rm MOS1}$	···	1.04(1)	1.04(1)	1.04(1)	1.03(1)	1.04(1)
XMM/EPIC-MOS2	$C_{\rm MOS2}$	···	0.97(1)	0.97(1)	0.97(1)	0.97(1)	0.97(1)
Fit statistic	χ^2_ν/dof	···	1.155/380	1.123/379	1.130/379	1.129/379	1.167/381

Notes.
[a] 1σ uncertainties in last digits shown in parentheses.
[b] Flux density at 1 keV in units of photons cm^{-2} s^{-1} keV^{-1}.
[c] $(3.02 \times 10^{-15}/4\pi D^2) \int n_e^2 dV$ in units of cm^{-5}.

Table 2
Spectral Fits with an Accreting Neutron-star Atmosphere[a]

Parameter	Symbol	Units	Hard Spectral Component				
			`cutoffpl`	`bknpow`	`comptt(disk)`	`comptt(sphere)`	`bremss`
Absorption and `zamp` parameters							
Absorption column	$N_{\rm H}$	10^{21} cm^{-2}	0.89(3)	0.87(6)	0.69(5)	0.69(5)	0.93(5)
Luminosity	$\log L_\infty/L_E$	···	−5.15(3)	−5.13(4)	−4.98(3)	−4.98(3)	−5.19(3)
Mass (fixed)	M	$M_\odot$	1.4	1.4	1.4	1.4	1.4
Radius (fixed)	R	km	12.4	12.4	12.4	12.4	12.4
Normalization	$K_{\rm zamp}$	10^{-3}	1.25(2)[b]	1.25(2)[b]	1.39(2)[b]	1.39(2)[b]	1.23(2)[b]
Hard spectral component parameters							
Normalization	K	10^{-4}	2.5(2)[b]	2.3(2)[b]	0.6(1)[b]	0.6(1)[b]	4.2(1)[c]
Photon index	Γ	···	1.08(9)	1.29(7)	···	···	···
Cutoff or break energy	E_c, E_b	keV	11.2(1.5)	5.9(3)	···	···	···
Photon index 2	Γ_2	···	···	2.03(5)	···	···	···
Electron temperature	kT_e	keV	···	···	7.3(1.6)	7.6(1.7)	17.9(1.0)
Seed temperature	kT_0	keV	···	···	0.81(4)	0.81(4)	···
Scattering optical depth	$\tau_{\rm es}$	···	···	···	3.6(6)	7.8(1.2)	···
Instrument multiplicative constants							
NuSTAR/FPMA	$C_{\rm FPMA}$	···	1.04(3)	1.03(3)	1.01(3)	1.01(3)	1.08(3)
NuSTAR/FPMB	$C_{\rm FPMB}$	···	1.07(3)	1.05(4)	1.04(4)	1.04(4)	1.10(4)
XMM/EPIC-pn (fixed)	$C_{\rm pn}$	···	1	1	1	1	1
XMM/EPIC-MOS1	$C_{\rm MOS1}$	···	1.04(1)	1.04(1)	1.03(1)	1.03(1)	1.03(1)
XMM/EPIC-MOS2	$C_{\rm MOS2}$	···	0.97(1)	0.97(1)	0.97(1)	0.97(1)	0.97(1)
Fit statistic	χ^2_ν/dof	···	1.156/380	1.129/379	1.109/379	1.109/379	1.162/381

Notes.
[a] 1σ uncertainties in last digits shown in parentheses.
[b] Flux density at 1 keV in units of photons cm^{-2} s^{-1} keV^{-1}.
[c] $(3.02 \times 10^{-15}/4\pi D^2) \int n_e^2 dV$ in units of cm^{-5}.

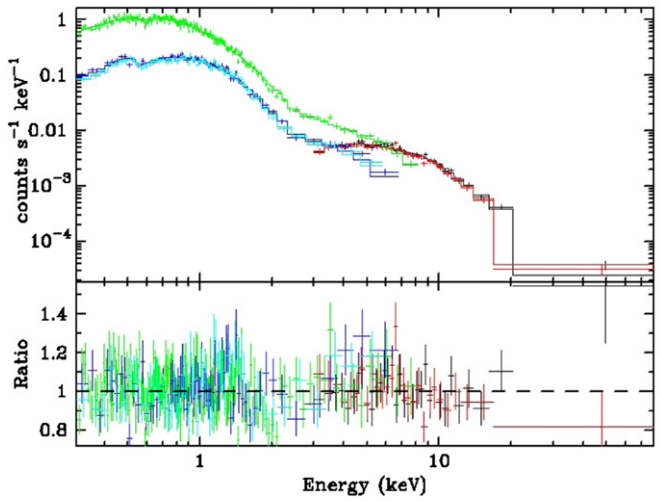

Figure 5. Count spectrum and model fit for our joint *XMM-Newton* and *NuSTAR* observation of Cen X-4, with the hard X-ray spectral cutoff included in the model. A bremsstrahlung model is shown: `tbabs*(nsatmos+bremss)`. The color scheme is the same as in Figure 4. The fit parameters are shown in Table 1.
(A color version of this figure is available in the online journal.)

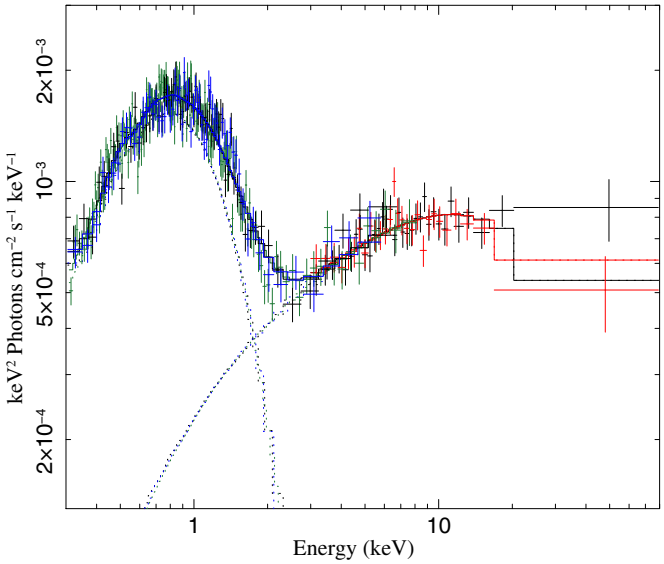

Figure 6. Unfolded νF_ν spectrum of Cen X-4 corresponding to the `tbabs*(nsatmos+bremss)` fit shown in Figure 5. The individual model components are denoted by the dotted lines. The cutoff of the hard spectral component above 10 keV is clearly visible.
(A color version of this figure is available in the online journal.)

$L_{\rm soft} = 6.6 \times 10^{32} D_{\rm kpc}^2$ erg s^{-1} (0.3–3 keV), the unabsorbed hard luminosity was $L_{\rm hard} = 4.0 \times 10^{32} D_{\rm kpc}^2$ erg s^{-1} (3–79 keV), and the total unabsorbed luminosity was $L_x = 1.1 \times 10^{33} D_{\rm kpc}^2$ erg s^{-1} (0.3–79 keV), where $D_{\rm kpc}$ is the source distance in kiloparsecs. For comparison with previous observations, the 0.5–10 keV unabsorbed luminosity was $6.4 \times 10^{32} D_{\rm kpc}^2$ erg s^{-1}. This is the highest 0.5–10 keV luminosity ever measured from Cen X-4 in quiescence. The next highest observation was 2.6 times fainter in 2001 (Campana et al. 2004b), and the faintest observation was 11.5 times fainter in 2009 (Cackett et al. 2010). The thermal (NS atmosphere) contribution to the 0.5–10 keV luminosity in our observation is 59%. This is consistent with previous observations, where the thermal fraction has always been 50%–60% (Cackett et al. 2010; Bernardini et al. 2013).

4. INTERPRETING THE SPECTRAL CUTOFF

We now discuss what can be inferred from our observed high-energy spectral cutoff. We introduce dimensionless variables for parameterizing the NS mass $M = 1.9\, M_{1.9}\, M_\odot$ and radius $R = 10\, R_{10}$ km. It is also convenient to scale the luminosity and accretion rate to the Eddington critical values:

$$L_E = 2.9 \times 10^{38}\, M_{1.9} \left(\frac{1+X}{1.7}\right)^{-1} \ {\rm erg\ s^{-1}} \qquad (1)$$

$$\dot{M}_E = 1.8 \times 10^{-8}\, R_{10} \left(\frac{1+X}{1.7}\right)^{-1} \ M_\odot\ {\rm yr^{-1}}\ , \qquad (2)$$

where $X = 0.7$ is the hydrogen mass fraction for cosmic abundances. Our observed luminosities can then be written as $L_{\rm soft}/L_E = 2.3 \times 10^{-6}\, M_{1.9}^{-1}$, $L_{\rm hard}/L_E = 1.4 \times 10^{-6}\, M_{1.9}^{-1}$, and $L_x/L_E = 3.8 \times 10^{-6}\, M_{1.9}^{-1}$. It is clear that the quiescent mass accretion rate $\dot{M}_{\rm NS}$ onto the NS must also be very low. We can set an upper limit by assigning all of the observed X-ray luminosity to accretion, $\dot{M}_{\rm NS} \leqslant L_x R/GM$. We then have $\dot{M}_{\rm NS}/\dot{M}_E \leqslant 3.7 \times 10^{-6}\, M_{1.9}^{-1}$. At such extremely low accretion rates, the outer accretion disk is likely to transition into a quasi-spherical, radiatively inefficient accretion flow (RIAF) at a transition radius $r_t \sim 10^4 R_{\rm Sch} \sim 6 \times 10^9\, M_{1.9}$ cm, where $R_{\rm Sch} = 2GM/c^2 = 5.6\, M_{1.9}$ km is the Schwarzschild radius (Narayan & Yi 1995; Narayan et al. 1998; Menou et al. 1999).

4.1. Comptonization

One way to explain a cutoff power-law spectrum is thermal Comptonization, where soft thermal seed photons (like those from the NS atmosphere) are Compton scattered from a corona of hot electrons. Menou & McClintock (2001) have previously argued that Comptonization of the NS atmosphere photons cannot account for the 1–10 keV power law observed in Cen X-4 because the observed luminosity in the power-law component is too high relative to the soft luminosity. We show here that a thermal Comptonization model for the hard spectral cutoff in Cen X-4 is not physically self-consistent, despite providing an acceptable fit to our observed spectrum. For simplicity, we consider the spherical geometry case; the results for a disk geometry are qualitatively similar.

Our `comptt` fits yielded an electron temperature of $kT_e = 6$–8 keV and an electron scattering optical depth of $\tau_{\rm es} = 8$–9 for a spherical geometry (see Tables 1 and 2). This is an unusually low kT_e for a Comptonized plasma, reflecting the observed spectral cutoff. It is likewise an unusually high $\tau_{\rm es}$; this follows from the fact that kT_e and $\tau_{\rm es}$ are inversely proportional for a fixed power-law index Γ (Titarchuk & Lyubarskij 1995). The optical depth in a corona of radius r_c is related to the electron density n_e by

$$\tau_{\rm es} = \sigma_T \int_R^{r_c} n_e(r) dr\ , \qquad (3)$$

where σ_T is the Thomson cross section. As we see below, it is our high value of $\tau_{\rm es}$ that makes it difficult to find a physically self-consistent Comptonization model.

4.1.1. Comptonization above the NS Atmosphere or the NS Magnetosphere

We begin by considering the possibility of a hot, optically thin layer above the NS atmosphere. Based on our measured $\tau_{\rm es}$, the electron density in the layer would be $n_e = 1.4 \times 10^{22}\, h_3^{-1}$ cm^{-3}, where $h = 10^3\, h_3$ cm is the thickness of the layer. This relatively dense scattering layer would itself be a source of significant thermal bremsstrahlung emission, with $kT_e \simeq 7$ keV. Despite the large scattering optical depth $\tau_{\rm es}$, the *effective* optical depth of the medium at 2 keV (including both scattering and free–free absorption) is only $\tau_{\rm eff} \simeq \sqrt{\tau_{\rm es}\tau_{\rm ff}} = 0.4\, h_3^{-1/2}$ (Rybicki & Lightman 1979), where $\tau_{\rm ff} = 0.02\, h_3^{-1}$ is the free–free absorption optical depth at 2 keV. (At higher energies, $\tau_{\rm ff}$ will be even smaller.) We can thus use the emissivity for optically thin thermal bremsstrahlung to compute the expected luminosity from the dense scattering layer, $3.6 \times 10^{36}\, h_3^{-1}$ erg s^{-1} $\approx 10^{-2}\, h_3^{-1}\, L_E$. This is orders of magnitude brighter than what we observe and can be ruled out.

We also consider a corona around the NS magnetosphere. In X-ray quiescence, we can scale the magnetospheric radius r_m to the corotation radius (where the Keplerian and stellar angular velocities are equal), which is given by

$$r_{\rm co} = \left(\frac{GMP^2}{4\pi^2}\right)^{1/3} = 39\, P_{3\,{\rm ms}}^{2/3}\, M_{1.9}^{1/3}\ {\rm km}\,, \qquad (4)$$

where we have written the (unknown) NS spin period as $P = 3\, P_{3\,{\rm ms}}$ ms. We assume a spherically symmetric corona with inner radius $r_{\rm co}$ and scale size $h \sim r_{\rm co}$. Then, following the calculations in the previous paragraph, we find an electron density of $n_e \simeq 4 \times 10^{18}\, (h/r_{\rm co})^{-1}$ cm^{-3}, an effective optical depth of $\tau_{\rm eff} \simeq \sqrt{\tau_{\rm es}\tau_{\rm ff}} \simeq 0.008\, (h/r_{\rm co})^{-1/2}$ at 2 keV, and a predicted bremsstrahlung luminosity from the scattering corona of $4 \times 10^{35}\, (h/r_{\rm co})^{-1}$ erg s^{-1} $\approx 10^{-3}\, (h/r_{\rm co})^{-1}\, L_E$. This is, again, orders of magnitude brighter than what we observe and can be ruled out.

4.1.2. Comptonization in the Accretion Flow

We next consider Comptonization in a RIAF-like spherical accretion flow with a radially uniform mass inflow rate $\dot{M}$ at infall velocity $v_r = \eta\sqrt{GM/r}$ (where $\eta \leqslant 1$). The electron density will vary with distance r from the NS as

$$n_e(r) = \frac{\dot{M}_{\rm NS}}{4\pi\,\eta\mu m_p (GMr^3)^{1/2}}\,, \qquad (5)$$

where μ is the mean molecular weight and m_p is the proton mass. We then find that the optical depth cannot exceed

$$\tau_{\rm es,max} \approx 10^{-3} \left(\frac{\eta}{0.1}\right)^{-1} \left(\frac{\dot{M}_{\rm NS}/\dot{M}_E}{4 \times 10^{-6}}\right), \qquad (6)$$

independent of r_c. This is orders of magnitude smaller than our `comptt` fit values for $\tau_{\rm es}$.

The only way to obtain higher optical depths is to assume that the mass inflow rate $\dot{M}$ varies with r in such a way that only a small amount of mass actually reaches the NS, with the remainder being expelled in some sort of outflow. For convenience, we parameterize $\dot{M}$ as a power law in r:

$$\dot{M}(r) = \left(\frac{r}{R}\right)^p \dot{M}_{\rm NS}, \qquad (7)$$

where R is the NS radius, $M_{\rm NS}$ is the mass accretion rate onto the NS, and $p > 0$. (The $p = 0$ case corresponds to the radially uniform inflow rate that we just dismissed.) This is the same parameterization used in the "ADIOS" (adiabatic inflow–outflow solution) model of Blandford & Begelman (1999). The electron density now varies as

$$n_e(r) = \frac{2}{\mu\eta\sigma_T R(1+X)}\sqrt{\frac{c^2R}{GM}} \left(\frac{\dot{M}_{\rm NS}}{\dot{M}_E}\right)\left(\frac{r}{R}\right)^{p-3/2} \qquad (8)$$

and the optical depth is

$$\tau_{\rm es} = \frac{2}{\mu\eta(1+X)}\sqrt{\frac{c^2R}{GM}} \left(\frac{\dot{M}_{\rm NS}}{\dot{M}_E}\right) \times \int_1^{r_c/R} \left(\frac{r}{R}\right)^{p-3/2} d\left(\frac{r}{R}\right). \qquad (9)$$

For ionized gas with cosmic abundances, we have $\mu = 0.6$ and $X = 0.7$. We require that $r_c < a$, where the binary separation is $a = 2.8 \times 10^{11}\, M_{1.9}^{1/3}$ cm (Frank et al. 2002; Shahbaz et al. 2014). This is equivalent to requiring that $r_c/R \lesssim 10^5$. Then taking $\dot{M}_{\rm NS}/\dot{M}_E = 4 \times 10^{-6}$ and $\tau_{\rm es} = 10$, we find $1.4 < p < 1.6$ for $0.1 < \eta < 1$. Even larger p values are required for smaller coronas. Such high p values yield high electron densities far from the NS, so the scattering cloud would again itself become a source of significant thermal bremsstrahlung emission. As an example, we consider the $p = 1.5$ (uniform density) case, for which $n_e = 4 \times 10^{14}$ cm^{-3}. The effective optical depth is $\tau_{\rm eff} \sim 10^{-4}$, so we expect optically thin bremsstrahlung emission. Taking $r_c/R = 10^5$ and $kT_e = 5$ keV, we predict a bremsstrahlung emission measure of $\int n_e^2 dV = 8 \times 10^{62}$ cm^{-3}, which corresponds to a luminosity of 8.5×10^{39} erg s^{-1} $\approx 40\, L_E$. This is nearly seven orders of magnitude brighter than the observed quiescent emission! We conclude that a thermal Comptonization model is not physically self-consistent for the hard spectral component in Cen X-4 in quiescence and can be ruled out.

4.2. Synchrotron Shock Emission

Another way of producing a cutoff power-law spectrum is through synchrotron emission. Radio pulsars dissipate their rotational energy via a relativistic wind comprising charged particles and Poynting flux (see Arons 2002; Gaensler & Slane 2006, and references therein). Quiescent NS/LMXB transients can turn on as radio pulsars under some circumstances (Stella et al. 1994); this has recently been observed in at least three cases (see Section 5.3). If Cen X-4 turned on as a radio pulsar during X-ray quiescence, then synchrotron shock emission from the radio pulsar wind interacting with intrabinary material or the interstellar medium (ISM) could produce a power-law X-ray spectrum (Campana et al. 1998a). The synchrotron power-law spectrum will have a high-energy exponential cutoff corresponding to the maximum energy of the electron population accelerated in the shock. This is generally thought to occur at energies of $\gtrsim$100 keV in pulsar wind shocks. Indeed, PSR J1023+0023, the only quiescent NS/LMXB in which synchrotron shock emission is definitely thought to have been observed, has an unbroken power-law spectrum out to at least 80 keV (Tendulkar et al. 2014). However, as we show below, it is possible to have lower cutoff energies in pulsar wind shocks.

4.2.1. Formalism

We begin by reviewing the formalism for the synchrotron shock scenario developed by Arons & Tavani (1993, hereinafter AT93) for the case of the eclipsing "black widow" millisecond pulsar PSR B1957+20. The pulsar wind is powered by spin-down of the pulsar with an energy loss rate set by magnetic dipole radiation:

$$\dot{E} = \frac{4\pi^2 I \dot{P}}{P^3}, \tag{10}$$

where P and $\dot{P}$ are the pulsar spin period and its derivative,[17] and we assume $I = 10^{45}$ g cm^2 for the NS moment of inertia. Because we do not know P and $\dot{P}$ for Cen X-4, we will scale the surface dipole magnetic field as $B = 10^8\, B_8$ G and the spin period as $P = 3\, P_{3\,\rm ms}$ ms, where we assume

$$B = \left(\frac{3c^3 I P \dot{P}}{8\pi^2 R^6}\right)^{1/2} \tag{11}$$

$$= 1.8 \times 10^8\, P_{3\,\rm ms}^{1/2} \left(\frac{\dot{P}}{10^{-20}}\right)^{1/2} \rm G\,. \tag{12}$$

Thus, for a millisecond pulsar, we have $\dot{P} = 0.3 \times 10^{-20}\, B_8^2\, P_{3\,\rm ms}^{-1}$ and $\dot{E} = 4.8 \times 10^{33}\, B_8^2\, P_{3\,\rm ms}^{-3}$ erg s^{-1}.

Upstream from the shock, the Lorentz factor in the wind is

$$\gamma_{\rm up} = 9 \times 10^4 \left(\frac{\eta_V}{0.3}\right)\left(\frac{Z}{A}\right) B_8\, P_{3\,\rm ms}^{-3/2}, \tag{13}$$

where we assume that the ions in the wind have charge Z and mass Am_p and are accelerated to a fraction $\eta_V \sim 0.3$ of the open-field line voltage of the NS. Possible ion values range from protons ($Z = A = 1$) to partially ionized iron ($Z \sim 3$, $A = 56$). The relative energetic contributions of Poynting flux and ions in the wind upstream of the shock are described by a magnetization parameter (Kennel & Coroniti 1984a):

$$\sigma = \frac{B_{\rm up}^2}{4\pi \rho_{\rm up} \gamma_{\rm up} c^2}, \tag{14}$$

where $B_{\rm up}$ and $\rho_{\rm up}$ are the magnetic field strength and density of the upstream wind. For a particle-dominated wind (like the one in the Crab Nebula), $\sigma \sim 10^{-3}$, and for a magnetically dominated wind, $\sigma \gg 1$. The upstream magnetic field strength can then be written as (Kennel & Coroniti 1984b)

$$B_{\rm up}(r_s) = \left(\frac{\sigma}{1+\sigma}\right)^{1/2} \left(\frac{\dot{E}}{r_s^2\, c\, f_p}\right)^{1/2}, \tag{15}$$

where $f_p = \Delta\Omega_p/4\pi$ is the fractional solid angle into which the wind is emitted. From the shock jump conditions, the downstream field strength is (Kennel & Coroniti 1984a)

$$B_{\rm down} \approx \begin{cases} 3\, B_{\rm up} & \text{for } \sigma \ll 1 \\ B_{\rm up} & \text{for } \sigma \gg 1. \end{cases} \tag{16}$$

The shock will give rise to a power-law electron population with energy distribution $N(\gamma) \propto \gamma^{-s}$ for $\gamma > \gamma_{\rm up}$, with $s \sim 2$. This will, in turn, produce a synchrotron radiation spectrum with photon number index $\Gamma \sim 1.5$ for photon energies above

$$E_{\rm min} \simeq 0.3\, \gamma_{\rm up}^2 \left(\frac{\hbar e B_{\rm down}}{m_e\, c}\right), \tag{17}$$

where e and m_e are the charge and mass of the electron. If radiative losses are negligible, these power laws will extend up to a cutoff at Lorentz factor

$$\gamma_m = \left(\frac{A}{Z}\right)\left(\frac{m_p}{m_e}\right)\gamma_{\rm up} = 2 \times 10^8 \left(\frac{\eta_V}{0.3}\right) B_8\, P_{3\,\rm ms}^{-3/2}, \tag{18}$$

and at photon energy

$$E_c = \gamma_m^2 \left(\frac{\hbar e B_{\rm down}}{m_e\, c}\right). \tag{19}$$

However, if radiative losses are significant, then the electron population will extend only to $\gamma_s < \gamma_m$. To find γ_s, we compare the acceleration time (AT93)

$$t_{\rm acc} = \left(\frac{A}{Z}\right)\frac{\gamma_{\rm up}\, m_p\, c}{e B_{\rm down}} \tag{20}$$

and the synchrotron loss time

$$t_s(\gamma) = \frac{6\pi m_e\, c}{\sigma_T\, B_{\rm down}^2\, \gamma} \tag{21}$$

and solve $t_{\rm acc} = t_s(\gamma_s)$. If $\gamma_s < \gamma_m$, then radiative losses are important, and the photon power law will only extend up to

$$E_c = \gamma_s^2 \left(\frac{\hbar e B_{\rm down}}{m_e\, c}\right). \tag{22}$$

Given the above formalism, we now consider two possible sites for the pulsar wind shock location.

4.2.2. Synchrotron Shock in the ISM

If the shock occurs where the pulsar wind is confined by ram pressure in the ISM, then the shock radius will be (Kulkarni & Hester 1988, AT93)

$$r_s = \left(\frac{\dot{E}}{4\pi f_p\, c\, m_p\, n\, v_p^2}\right)^{1/2} \tag{23}$$

$$= 4 \times 10^{15}\, f_p^{-1/2}\, n_1^{-1}\, v_{200}^{-2}\, B_8\, P_{3\,\rm ms}^{-3/2} \rm cm, \tag{24}$$

where $n = n_1$ cm^{-3} is the ISM particle density and $v_p = 200\, v_{200}$ km s^{-1} is the pulsar space velocity (Shahbaz et al. 2014). At this large distance from the NS, we assume that $\sigma \ll 1$ (Arons 2002). Then, the upstream magnetic field strength is

$$B_{\rm up}(r_s) = 3 \times 10^{-6} \left(\frac{\sigma}{10^{-3}}\right)^{1/2} n_1\, v_{200}^2\, \rm G, \tag{25}$$

and the magnetic field downstream of the shock is $B_{\rm down} \approx 3 B_{\rm up}$. Radiative losses are negligible in such a weak field, so the expected synchrotron power-law spectrum will extend from

$$E_{\rm min} = 3 \times 10^{-7} \left(\frac{\sigma}{10^{-3}}\right)^{1/2} \left(\frac{\eta_V}{0.3}\right)^2 \left(\frac{Z}{A}\right)^2 \times n_1\, v_{200}^2\, B_8^2\, P_{3\,\rm ms}^{-3}\, \rm keV \tag{26}$$

[17] Note that $\dot{P}$ is the spin period derivative due to magnetic dipole spin-down alone, in the absence of any accretion torques.

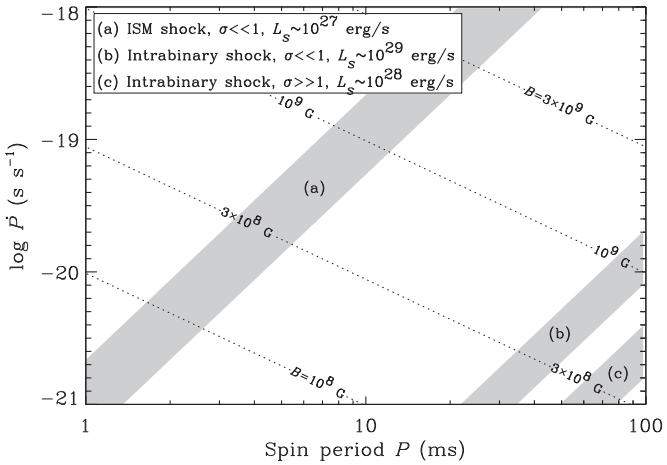

Figure 7. Regions with low predicted cutoff energy E_c for a synchrotron shock spectrum, displayed as a function of the radio pulsar spin period P and period derivative $\dot{P}$; P and $\dot{P}$ are not known for Cen X-4. The dotted lines show contours of constant pulsar magnetic field strength B (see Equation (12)). The shaded regions have E_c in the 5–20 keV range, consistent with the observed power-law cutoff energy in Cen X-4, and correspond to the three cases listed in the box on the upper left. Radiative losses are negligible in all of these regions ($\gamma_s > \gamma_m$). Contours of constant E_c and constant synchrotron luminosity L_s have the same slope on the P–$\dot{P}$ plane. In all three regions, the predicted L_s is orders of magnitude too small to explain the observed power-law luminosity ($\sim 10^{32}$ erg s^{-1}) in Cen X-4. Additional regions, corresponding to the intrabinary shock cases where radiative losses dominate ($\gamma_s < \gamma_m$), are not shown; they lie in an unphysical part of the phase space ($P \lesssim 1$ ms and $B \gtrsim 10^9$ G) for $E_c < 20$ keV. All calculations were done with $\eta_V = 0.3$, $\epsilon_a = 0.2$, and $f_{\rm geom} = 0.05$.

to a cutoff at

$$E_c = 3.3 \left(\frac{\sigma}{10^{-3}}\right)^{1/2} \left(\frac{\eta_V}{0.3}\right)^2 n_1\, v_{200}^2 \times B_8^2\, P_{3\,\rm ms}^{-3}\,\rm keV. \quad (27)$$

The ISM shock model produces a cutoff energy consistent with our observed spectrum for a reasonable range of pulsar parameters, as shown in shaded region (a) of Figure 7. However, the predicted synchrotron emission corresponding to that region is orders of magnitude weaker than our observed power-law luminosity ($\sim 10^{32}$ erg s^{-1}). Scaling to P and B values that lie in the central strip of region (a) in Figure 7, the expected 0.3–20 keV synchrotron luminosity from the ISM shock is (AT93, Equation (16))

$$L_s \simeq 2\times10^{27} \left(\frac{\sigma}{10^{-3}}\right)\left(\frac{\epsilon_a}{0.2}\right)\left(\frac{\eta_V}{0.3}\right)\left(\frac{n_1}{f_p^3}\right)^{1/2} v_{200} \times \left(\frac{f_{\rm band}}{0.8}\right) B_8^4 \left(\frac{P}{2\,\rm ms}\right)^{-6} \rm erg\,s^{-1}, \quad (28)$$

where ϵ_a is the conversion efficiency of pulsar wind luminosity into particle acceleration in the shock, and $f_{\rm band}$ is the fraction of the bolometric synchrotron luminosity that lies in the 0.3–20 keV band:

$$f_{\rm band} \simeq \left[\frac{\min(20\,\rm keV,\, E_c)}{E_c}\right]^{1/2} - \left[\frac{0.3\,\rm keV}{E_c}\right]^{1/2}. \quad (29)$$

Note that the contours of constant E_c and constant L_s have the same slope in Figure 7, so the numerical prefactor in Equation (28) characterizes the entire length of the shaded region. We conclude that synchrotron emission from a shock in the ISM cannot explain the observed hard X-ray spectrum in Cen X-4.

4.2.3. Intrabinary Shock

Another possibility is that the pulsar wind collides with material lost from the binary companion or the accretion flow at a shock radius $r_s \sim a$, where the magnetic field is considerably stronger than in the ISM case. In PSR J1023+0038, the intrabinary shock was modeled as occurring near the inner Lagrangian (L_1) point (Bogdanov et al. 2011); in Cen X-4, the L_1 point lies at $r \approx 0.67a$. It is unclear whether the pulsar wind would be particle dominated or not in an intrabinary shock relatively close to the pulsar. Arons (2002) points out that theory predicts $\sigma \gg 1$ at the pulsar light cylinder, but that observations indicate $\sigma \ll 1$ in observed pulsar wind nebulae produced by ISM shocks, and that it is not clear how or where the transition from one regime to the other occurs. We note that Bogdanov et al. (2011) inferred $\sigma \gg 1$ for the intrabinary shock in PSR J1023+0038. We therefore consider both the $\sigma \ll 1$ and $\sigma \gg 1$ cases here.[18]

Scaling to the binary separation in Equation (15), the upstream magnetic field is now

$$B_{\rm up}(r_s) = \left(\frac{\sigma}{1+\sigma}\right)^{1/2} \left(\frac{\dot{E}}{a^2\, c\, f_p}\right)^{1/2} \left(\frac{r_s}{a}\right)^{-1} \quad (30)$$

$$= 0.04 \left(\frac{\sigma}{10^{-3}}\right)^{1/2} f_p^{-1/2} \left(\frac{r_s}{a}\right)^{-1} \left(\frac{a}{a_0}\right)^{-1} \times B_8\, P_{3\,\rm ms}^{-3/2}\rm G, \quad \text{for } \sigma \ll 1 \quad (31)$$

$$= 1.4\, f_p^{-1/2} \left(\frac{r_s}{a}\right)^{-1} \left(\frac{a}{a_0}\right)^{-1} \times B_8\, P_{3\,\rm ms}^{-3/2}\rm G, \quad \text{for } \sigma \gg 1, \quad (32)$$

where $a_0 = 2.8\times10^{11}$ cm. The downstream field $B_{\rm down}$ is given by Equation (16). From Equation (17), the lower energy bound for the synchrotron power law is

$$E_{\rm min} = 0.003 \left(\frac{\sigma}{10^{-3}}\right)^{1/2} f_p^{-1/2} \left(\frac{\eta_V}{0.3}\right)^2 \left(\frac{r_s}{a}\right)^{-1} \left(\frac{a}{a_0}\right)^{-1} \times \left(\frac{Z}{A}\right)^2 B_8^3\, P_{3\,\rm ms}^{-9/2}\,\rm keV, \quad \text{for } \sigma \ll 1 \quad (33)$$

$$= 0.04\, f_p^{-1/2} \left(\frac{\eta_V}{0.3}\right)^2 \left(\frac{r_s}{a}\right)^{-1} \left(\frac{a}{a_0}\right)^{-1} \times \left(\frac{Z}{A}\right)^2 B_8^3\, P_{3\,\rm ms}^{-9/2}\,\rm keV, \quad \text{for } \sigma \gg 1. \quad (34)$$

[18] We follow Stappers et al. (2003) and Bogdanov et al. (2011) in taking this approach. However, it is not clear that the synchrotron shock model is viable for $\sigma \gg 1$. Kennel & Coroniti (1984a) wrote: "Large-σ shocks are effectively weak... Only when $\sigma \lesssim 0.1$ can a significant fraction of the total energy flux upstream be converted into thermal energy downstream and thereafter into synchrotron luminosity."

The upper bound depends on whether or not radiative losses are important, which is set by the ratio

$$\frac{\gamma_s}{\gamma_m} = 36 \left(\frac{\sigma}{10^{-3}}\right)^{-1/2} f_p^{1/2} \left(\frac{\eta_V}{0.3}\right)^{-2} \left(\frac{r_s}{a}\right) \left(\frac{a}{a_0}\right) \times B_8^{-3} P_{3\,\mathrm{ms}}^{9/2}, \quad \text{for } \sigma \ll 1 \tag{35}$$

$$= 3 f_p^{1/2} \left(\frac{\eta_V}{0.3}\right)^{-2} \left(\frac{r_s}{a}\right) \left(\frac{a}{a_0}\right) \times B_8^{-3} P_{3\,\mathrm{ms}}^{9/2}, \quad \text{for } \sigma \gg 1. \tag{36}$$

From Equations (19) and (22), the cutoff energy for the $\sigma \ll 1$ case is then

$$E_c = 4.5 \times 10^4 \left(\frac{\sigma}{10^{-3}}\right)^{1/2} f_p^{-1/2} \left(\frac{\eta_V}{0.3}\right)^{2} \left(\frac{r_s}{a}\right)^{-1} \times \left(\frac{a}{a_0}\right)^{-1} B_8^3 P_{3\,\mathrm{ms}}^{-9/2}\ \mathrm{keV}, \quad \text{for } \gamma_s > \gamma_m \tag{37}$$

$$= 5.6 \times 10^7 \left(\frac{\sigma}{10^{-3}}\right)^{-1/2} f_p^{1/2} \left(\frac{\eta_V}{0.3}\right)^{-2} \left(\frac{r_s}{a}\right) \times \left(\frac{a}{a_0}\right) B_8^{-3} P_{3\,\mathrm{ms}}^{9/2}\ \mathrm{keV}, \quad \text{for } \gamma_s < \gamma_m, \tag{38}$$

and for the $\sigma \gg 1$ case it is

$$E_c = 5.2 \times 10^5 f_p^{-1/2} \left(\frac{\eta_V}{0.3}\right)^{2} \left(\frac{r_s}{a}\right)^{-1} \left(\frac{a}{a_0}\right)^{-1} \times B_8^3 P_{3\,\mathrm{ms}}^{-9/2}\ \mathrm{keV}, \quad \text{for } \gamma_s > \gamma_m \tag{39}$$

$$= 4.7 \times 10^6 f_p^{1/2} \left(\frac{\eta_V}{0.3}\right)^{-2} \left(\frac{r_s}{a}\right) \left(\frac{a}{a_0}\right) \times B_8^{-3} P_{3\,\mathrm{ms}}^{9/2}\ \mathrm{keV}, \quad \text{for } \gamma_s < \gamma_m. \tag{40}$$

The intrabinary shock model with $\gamma_s > \gamma_m$ is able to produce a cutoff energy consistent with our observed spectrum for a reasonable range of pulsar parameters, as shown in shaded regions (b) and (c) of Figure 7. However, again, the predicted synchrotron luminosity corresponding to those regions is orders of magnitude smaller than our observed power-law luminosity. The expected 0.3–20 keV synchrotron luminosity from an intrabinary shock is (AT93, Equation (24))

$$L_s \simeq \epsilon_a \dot{E}\, f_{\mathrm{band}}\, f_{\mathrm{geom}}, \tag{41}$$

where f_{geom} is the fraction of the pulsar wind intercepted by intrabinary material. By analogy to PSR J1023+0038, we expect f_{geom} to be in the range 0.01–0.1 (Bogdanov et al. 2011). Scaling to P and B values inside the shaded regions, we thus have

$$L_s \simeq 2 \times 10^{29} \left(\frac{f_{\mathrm{band}}}{0.8}\right) \left(\frac{\epsilon_a}{0.2}\right) \left(\frac{f_{\mathrm{geom}}}{0.05}\right) \times \left(\frac{B}{3 \times 10^8\ \mathrm{G}}\right)^2 \left(\frac{P}{40\ \mathrm{ms}}\right)^{-3} \mathrm{erg\ s^{-1}} \tag{42}$$

for the $\gamma_s > \gamma_m$, $\sigma \ll 1$ case [region (b)], and

$$L_s \simeq 3 \times 10^{28} \left(\frac{f_{\mathrm{band}}}{0.8}\right) \left(\frac{\epsilon_a}{0.2}\right) \left(\frac{f_{\mathrm{geom}}}{0.05}\right) \times \left(\frac{B}{3 \times 10^8\ \mathrm{G}}\right)^2 \left(\frac{P}{70\ \mathrm{ms}}\right)^{-3} \mathrm{erg\ s^{-1}}, \tag{43}$$

for the $\gamma_s > \gamma_m$, $\sigma \gg 1$ case [region (c)]. The cases where radiative losses dominate ($\gamma_s < \gamma_m$) only give low enough cutoff energies for an unphysical set of pulsar parameters ($P \lesssim 1$ ms with $B \gtrsim 10^9$ G, beyond the upper left corner of Figure 7), and they predict a synchrotron luminosity at least two orders of magnitude *larger* than what we observe. Taken together, we conclude that synchrotron emission from an intrabinary shock cannot explain the cutoff power-law spectrum in Cen X-4.

4.3. Bremsstrahlung

A third way of modeling our cutoff spectrum is through thermal bremsstrahlung emission from an optically thin cloud of hot electrons. Our bremsstrahlung fits (see Tables 1 and 2) yielded an electron temperature kT_e =18 keV and an emission measure

$$\int n_e^2\, dV = 1.6 \times 10^{55}\, D_{\mathrm{kpc}}^2\ \mathrm{cm^{-3}}. \tag{44}$$

We examine two different possibilities for the emission site.

4.3.1. Emission from above the NS Atmosphere

We again consider the possibility of a hot, optically thin layer above the NS atmosphere with geometric thickness $h = 10^3\, h_3$ cm. The observed emission measure requires an electron density of

$$n_e = 3.6 \times 10^{19}\, h_3^{-1/2}\, D_{\mathrm{kpc}}\ \mathrm{cm^{-3}}. \tag{45}$$

This implies a free–free absorption optical depth of only $\tau_{\mathrm{ff}} \simeq 10^{-8}$ at 2 keV, which is self-consistent for optically thin thermal bremsstrahlung emission. In this scenario, both the soft (thermal) emission and the hard (bremsstrahlung) emission are formed in or above the NS atmosphere. This can thus easily account for the fact that the soft and hard emission are observed to vary together on short timescales, with no detectable time lag.

Deufel et al. (2001) calculated the spectrum of an unmagnetized NS atmosphere accreting at low rates through a RIAF flow. Their work differs from the low-$\dot{M}$ case considered by Zampieri et al. (1995, see also Section 3.2) in that it includes Coulomb heating of the atmosphere by energetic protons in the RIAF flow. Interestingly, they *predict* a hot, optically thin surface layer above the NS atmosphere with $kT_e \approx 50$ keV and with significant bremsstrahlung emission expected for a certain range of $\dot{M}_{\mathrm{NS}}$, in addition to the soft thermal emission from the NS surface. Their most detailed calculations were made assuming a proton temperature of $0.5kT_{\mathrm{vir}}$, where T_{vir} is the virial temperature. For this case, they found that the bremsstrahlung emission is comparable in strength to the thermal component when $\dot{M}_{\mathrm{ns}} \gtrsim 10^{-2}\dot{M}_E$, but that it becomes negligible when $\dot{M}_{\mathrm{ns}} \lesssim 10^{-4}\dot{M}_E$. By comparison, our observation of Cen X-4 measured comparable luminosity in the two components when the accretion rate was much lower, $\dot{M}_{\mathrm{ns}} \leqslant 3.7 \times 10^{-6}\dot{M}_E$. This is a factor of 10^4 discrepancy with the Deufel et al. (2001) calculation.

One way of reconciling this is to invoke magnetic channeling of the quiescent accretion flow onto the NS polar caps, thus increasing the local accretion rate per unit area. However, this

would require very small polar caps with area $A_{\rm cap} \sim 10^{-4}\,\pi R^2$. The measured spectral parameters of the soft thermal component in Cen X-4 are not consistent with such small polar caps (see Tables 1 and 2). On the contrary, they suggest that the thermal emission arises from a significant fraction of the stellar surface. Another alternative is to reexamine the assumptions of the Deufel et al. (2001) calculation because the expected bremsstrahlung luminosity must depend on the details of the Coulomb heating of the atmosphere. The authors found that, for a fixed accretion rate, reducing the proton temperature increases the heating in the upper atmosphere because the protons do not penetrate as deeply. However, they did not investigate this case in detail, so it is not clear whether a physically reasonable choice of proton temperature can produce significant bremsstrahlung emission at accretion rates as low as we observed in Cen X-4.

We conclude that bremsstrahlung emission from a hot layer above the NS atmosphere is consistent with our observed spectral cutoff. However, it is not yet clear how to produce sufficient luminosity to match our data based on existing theoretical models for RIAF accretion onto NSs.

4.3.2. Emission from the RIAF Accretion Flow

As another alternative, we again assume that $\dot{M}$ varies with distance from the NS according to Equation (7) and use Equation (8) for n_e. Then, taking $\mu = 0.6$ and $X = 0.7$ for ionized gas with cosmic abundances, the expected emission measure for a cloud of radius r_c is

$$\int n_e^2\, dV = \frac{8\pi R}{p\eta^2\sigma_T^2}\left(\frac{c^2 R}{GM}\right)\left(\frac{\dot{M}_{\rm NS}}{\dot{M}_E}\right)^2\left(\frac{r_c}{R}\right)^{2p}. \quad (46)$$

Equating this to Equation (44), we find that

$$\frac{r_c}{R} \approx 10^{4/p}\, p^{1/2p}\, D_{\rm kpc}^{1/p}\left(\frac{\eta}{0.1}\right)^{1/p} \times \left(\frac{\dot{M}_{\rm NS}/\dot{M}_E}{4\times 10^{-6}}\right)^{-1/p}, \quad (47)$$

which sets the scale for the bremsstrahlung emission region in units of the NS radius R. Requiring $r_c < a$ or equivalently $r_c/R \lesssim 10^5$, we find that $p \gtrsim 0.8$. Alternatively, if we require that the cloud lies inside the RIAF transition radius ($r_c < r_t$ or $r_c/R \lesssim 10^4$), then we find that $p \gtrsim 1$. In either case, only a small fraction $(r_c/R)^{-p} \lesssim 10^{-4}$ of the mass transferred reaches the NS in quiescence; the rest accumulates at large r or is expelled. In particular, we note that much of the bremsstrahlung emission is coming from electrons at large r. For $p = 1$, the electron density $n_{\rm e}$ ranges from 10^{14} cm^{-3} near the NS to 10^{12} cm^{-3} near r_c.

This scenario is able to self-consistently account for the observed bremsstrahlung luminosity. However, it is challenging to explain the short ($\lesssim$30 s) lag time observed between the soft and hard flux variability in the X-ray light curve (see Section 3.1). Presumably, the hard flares would arise from mass fluctuations in the RIAF flow, and the soft flares would arise when those fluctuations reach the NS surface. The shortest possible timescale between the soft and hard flares is then the free-fall timescale from r_c,

$$t_{\rm ff} = 60\, M_{1.9}^{-1/2}\left(\frac{r_c}{10^4\, R}\right)^{3/2}\ {\rm s}. \quad (48)$$

This is only marginally consistent with our upper limit on the lag time. We conclude that bremsstrahlung emission from the RIAF flow is consistent with our observed spectral cutoff and luminosity, but placing this emission far from the NS is difficult to reconcile with the fact that the soft and hard emission vary together on short timescales.

5. DISCUSSION

5.1. The Spectral Cutoff in Cen X-4

We have measured a cutoff in the hard X-ray power-law spectrum of Cen X-4 that can be fit with an exponential cutoff at around 10 keV or a bremsstrahlung spectrum with $kT_e = 18$ keV. This is the first detection of a power-law cutoff in this source class, and it finally permits a more detailed investigation of the origin of the hard component in quiescent NS/LMXBs. We were able to rule out both thermal Comptonization and synchrotron shock emission as the origin of the spectral cutoff. Instead, the hard X-ray spectrum can be understood as bremsstrahlung emission, arising either from a hot, optically thin corona above the NS atmosphere or from hot electrons in an optically thin RIAF. The NS atmosphere scenario has the advantage that it can easily explain why the soft and hard emissions vary together on short timescales, while the RIAF scenario has the advantage that it can self-consistently account for the observed luminosity.

The 18 keV electron temperature for the `bremss` model is much lower than either the ~50 keV electron temperature predicted for the hot layer above an NS atmosphere (Deufel et al. 2001) or the $\gtrsim$100 keV electron temperature expected in a RIAF flow around a BH (Mahadevan & Quataert 1997). This may be due to Compton cooling of the bremsstrahlung electrons by the soft X-ray photons from the NS atmosphere, in which case we would expect T_e to depend upon the soft X-ray luminosity $L_{\rm soft}$. The absence of a detectable Compton emission component is not problematic. The Compton radiative power density is

$$P_C = \sigma_T\, n_e\left(\frac{4kT_e}{m_e c^2}\right)\left(\frac{L_{\rm soft}}{4\pi r^2}\right). \quad (49)$$

The resulting inverse Compton luminosity is

$$L_{C,{\rm atm}} = 5\times 10^{29}\, h_3^{1/2}\left(\frac{kT}{18\,{\rm keV}}\right) \times \left(\frac{L_{\rm soft}/L_E}{2\times 10^{-6}}\right){\rm erg\ s^{-1}} \quad (50)$$

for cooling above the NS atmosphere, or

$$L_{C,{\rm RIAF}} = 3\times 10^{30}\left(\frac{\eta}{0.1}\right)^{-1}\left(\frac{kT}{18\,{\rm keV}}\right)\left(\frac{\dot{M}_{\rm NS}/\dot{M}_E}{4\times 10^{-6}}\right) \times \left(\frac{L_{\rm soft}/L_E}{2\times 10^{-6}}\right){\rm erg\ s^{-1}} \quad (51)$$

for cooling in the accretion flow. In either case, the Compton luminosity is no more than a few percent of the overall source luminosity and thus essentially undetectable in our spectrum.

It is interesting to consider whether the flares observed in the X-ray light curve might be expected to affect the electron temperature (and thus the cutoff energy). The Compton cooling timescale is $t_C = (3/2)n_e kT_e/P_C$. For emission above the NS atmosphere, this yields

$$t_{C,{\rm atm}} = 1\times 10^{-2}\, M_{1.9}^{-1}\left(\frac{L_{\rm soft}/L_E}{2\times 10^{-6}}\right)^{-1}{\rm s}, \quad (52)$$

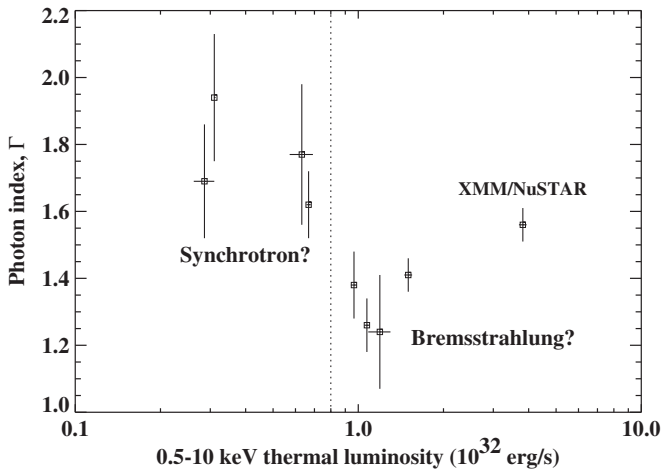

Figure 8. Hard X-ray power-law photon index (2–10 keV) vs. unabsorbed 0.5–10 keV thermal luminosity for deep observations of Cen X-4 (see Table 3). The *XMM/NuSTAR* point is from a `tbabs*(nsatmos+powerlaw)` fit to the 0.3–10 keV data only. The thermal luminosity $L_{\rm th}$ is computed for a distance of 1 kpc. For $L_{\rm th} \gtrsim 10^{32}\, D^2_{\rm kpc}$ erg s^{-1}, the data are roughly consistent with a trend of steeper power-law slope for higher $L_{\rm th}$, as expected for bremsstrahlung emission, if we assume that kT_e is reduced from 50–100 keV via Compton cooling by thermal photons. In energy bandpasses well below kT_e, a bremsstrahlung spectrum is a $\Gamma = 1$ power law. The large Γ measured at the lowest thermal luminosities may indicate a transition to synchrotron shock emission at extremely low $\dot{M}$.

so the cooling is nearly instantaneous. For this scenario, we might expect to measure spectral changes in the *NuSTAR* band ($\gtrsim$10 keV) during the flares, although we did not have a sufficiently high signal-to-noise ratio to do this with our observation. By contrast, emission in the RIAF gives

$$t_{C,\rm RIAF} = 1 \times 10^6\, M_{1.9}^{-1} \left(\frac{r}{10^4\, R}\right)^2 \left(\frac{L_{\rm soft}/L_E}{2 \times 10^{-6}}\right)^{-1} {\rm s}\,, \quad (53)$$

so in this case short-term flaring behavior will not result in significant Compton cooling of the bremsstrahlung electrons in the RIAF flow. This might provide an avenue for discriminating between the two scenarios.

On longer timescales (months to years), the fact that the slope of the hard X-ray power-law spectrum in Cen X-4 was observed to vary from epoch to epoch over the course of two decades (Cackett et al. 2010) makes it unlikely that the 18 keV bremsstrahlung spectrum we have measured is a constant feature of the source in quiescence. In fact, we can demonstrate that the hard X-ray cutoff energy in Cen X-4 is likely variable by noting that the departure of the hard X-ray spectrum from an unbroken power law above $\simeq$6 keV is evident in our 2013 *XMM-Newton* spectrum alone, even without including the *NuSTAR* data. The shape of an 18 keV bremsstrahlung spectrum will show noticeable curvature below 10 keV. On the other hand, all previous deep observations of Cen X-4 in the 0.5–10 keV band are consistent with an unbroken hard X-ray power-law spectrum, indicating a higher cutoff energy for those observations. All of these observations occurred at significantly lower luminosity (see Figure 8). We would expect a lower thermal luminosity to result in reduced Compton cooling of the bremsstrahlung electrons and hence a higher electron temperature, consistent with a higher cutoff energy.

Moreover, we would expect the 2–10 keV power-law slope to vary systematically with the thermal luminosity $L_{\rm th}$. For energy bandpasses far below kT_e, a bremsstrahlung spectrum is a $\Gamma = 1$ power law (see, e.g., Rybicki & Lightman 1979); as one approaches the cutoff at kT_e from below, the effective Γ over a fixed bandpass increases as the spectrum begins to gradually roll over. Thus, if we assume that $kT_e \gtrsim$ 50–100 keV in the absence of Compton cooling, then a Compton-cooled bremsstrahlung model predicts that Γ should be close to 1 at low $L_{\rm th}$ and should increase as $L_{\rm th}$ rises and kT_e falls. This relationship will eventually break down when kT_e gets sufficiently low because an unbroken power law no longer provides even a rough fit to a sharp spectral cutoff. The archival data roughly support this picture for $L_{\rm th} \gtrsim 10^{32}\, D^2_{\rm kpc}$ erg s^{-1}. In Figure 8, we plot Γ versus $L_{\rm th}$ for deep quiescent observations of Cen X-4 made since 1994, including our observation.[19] These observations are listed in Table 3; the archival spectra are collected from Cackett et al. (2010) and Cackett et al. (2013). The trend of the observations in Figure 8 with $L_{\rm th} \gtrsim 10^{32}\, D^2_{\rm kpc}$ erg s^{-1} is roughly consistent with our expectation for a Compton-cooled bremsstrahlung model.

At the lowest thermal luminosities, however, Γ jumps to higher values. The abrupt change is suggestive of a spectral transition to a different emission mechanism. Given the extremely low luminosities, one might consider coronal X-ray emission from the companion star (Bildsten & Rutledge 2000), but the observed spectral shapes for these observations were not consistent with coronal emission (Cackett et al. 2010, 2013). Instead, we suggest that this may indicate a transition to synchrotron shock emission at the lowest luminosities. We discuss this further in Section 5.3.

Table 3
Hard X-Ray Power-law Spectra of Deep Cen X-4 Observations[a]

Start Date	Mission	Exposure (ks)	$L_{\rm th}$[b] (10^{32} erg s^{-1})	Γ	Ref.
1994 Feb 27	*ASCA*	39	1.19(11)	1.24(17)	1
2001 Aug 20	*XMM*	53	1.50(5)	1.41(5)	1
2003 Mar 1	*XMM*	78	1.07(2)	1.26(8)	1
2009 Jan 16	*Suzaku*	147	0.29(2)	1.69(17)	1
2010 Aug 25	*XMM*	21	0.63(6)	1.77(21)	2
2010 Sep 4	*XMM*	23	0.67(1)	1.62(10)	2
2011 Jan 24	*XMM*	15	0.97(2)	1.38(10)	2
2011 Jan 31	*XMM*	14	0.31(1)	1.94(19)	2
2013 Jan 20	*XMM+NuSTAR*[c]	27/114	3.8(1)	1.56(5)	3

Notes. All archival data fit to `phabs*(nsatmos+powerlaw)` model. *Chandra* observations excluded owing to possible photon pileup.
[a] 1σ uncertainties in last digits shown in parentheses.
[b] 0.5–10 keV thermal luminosity assuming $D = 1$ kpc.
[c] Fit only to 0.3–10 keV data using `tbabs*(nsatmos+powerlaw)` model, with no power-law break.
References (1) Cackett et al. 2010 and references therein; (2) Cackett et al. 2013; (3) this work.

5.2. The Nature of Low-$\dot{M}$ Accretion

As in most quiescent transient NS/LMXBs, a basic requirement for Cen X-4 is that most of the accretion flow does not reach the NS because the inferred $\dot{M}_{\rm NS}$ is substantially smaller than the binary mass transfer rate $\dot{M}_T \sim 0.01 \dot{M}_E$ expected for a Roche-lobe–filling main-sequence donor in a 15.1 hr binary (e.g., King et al. 1996). There may be several mechanisms that contribute to

[19] We exclude observations made with *Chandra*/ACIS, which may be subject to pileup effects. We note that the Γ values found by Cackett et al. (2010) for these observations are much smaller than for any other observations, as would be expected if there is significant pileup. We will reexamine these data elsewhere.

this. First of all, the disk instability model for LMXB transients predicts that most of the accretion flow during X-ray quiescence builds up in the outer accretion disk until a thermal instability ensues, causing an outburst (see Lasota 2001). At low $\dot{M}$, the outer disk will transition into a quasi-spherical RIAF flow at r_t. It has previously been noted that RIAF models for quiescent NS transients require that most of the RIAF flow is somehow prevented from reaching the NS (Asai et al. 1998; Menou et al. 1999). One way of achieving this is the ADIOS-like outflow that we discussed in Section 4.3.2.

Another possibility is that most of the flow reaching the NS magnetosphere is centrifugally inhibited by the magnetic "propeller effect" (Illarionov & Sunyaev 1975; Ustyugova et al. 2006). This occurs when the magnetosphere extends beyond the corotation radius (see Equation (4)). We define the magnetospheric radius r_m as the location where the magnetic and material stresses are equal:

$$r_m = \xi \left(\frac{\mu_m^4}{GM\dot{M}^2} \right)^{1/7} \tag{54}$$

$$= 31\, \xi\, B_8^{4/7}\, M_{1.9}^{-1/7}\, R_{10}^{10/7} \times \left(\frac{\dot{M}/\dot{M}_E}{0.01} \right)^{-2/7} \text{km}, \tag{55}$$

where μ_m is the magnetic dipole moment of the NS, ξ is an order unity constant that depends upon the details of the accretion flow near the magnetosphere (see, e.g., Psaltis & Chakrabarty 1999), and the usual $R^{12/7}$ scaling is modified by the R dependence of $\dot{M}_E$. In the propeller regime, $r_m > r_{\rm co}$. For ordinary thin-disk magnetic accretion, the disk extends to the magnetosphere, and the accretion is entirely shut off in this regime. However, for a RIAF flow onto a millisecond pulsar, r_m will generally lie inside the transition radius r_t, so the flow onto the magnetosphere will be quasi-spherical. In this geometry, a small fraction of the flow is able to reach the NS despite the centrifugal barrier present in the propeller regime (Menou et al. 1999). Whether material is expelled in a strong or weak outflow, or else accumulates outside $r_{\rm co}$ (e.g., a "dead" disk), depends upon details of the disk–magnetosphere interaction (Spruit & Taam 1993; D'Angelo & Spruit 2010, 2012; Lii et al. 2014). However, observationally, Bernardini et al. (2013) have shown that a strong propeller outflow can likely be ruled out in Cen X-4.

Our observations support the conclusion of Bernardini et al. (2013) that low-level accretion is occurring during X-ray quiescence in Cen X-4, indicating that a small fraction of the accretion flow must eventually reach the NS. However, it remains unclear what combination of the above mechanisms ultimately controls what that fraction is.

5.3. Comparison to Other Low-$\dot{M}$ Systems

After Cen X-4, the next brightest well-studied quiescent NS/LMXB transient is Aql X-1. Unlike Cen X-4, Aql X-1 has a relatively short recurrence timescale of 1–2 yr. There have been several recent studies of its quiescent emission (Cackett et al. 2011; Coti Zelati et al. 2014; Sakurai et al. 2014), all observing a soft thermal component and hard power-law component with no cutoff. Sakurai et al. (2014) argue that, for their 2007 *Suzaku* observations ($L/L_E = [3\text{–}9] \times 10^{-5}\, M_{1.9}$ for an assumed distance of 5.2 kpc), the most appropriate model for the hard component is Comptonization in either an optically thin ($\tau_{\rm es} \simeq 0.3$), very hot ($kT_e > 100$ keV) corona or an optically thick ($\tau_{\rm es} > 3$), somewhat cooler ($kT_e \sim 50$ keV) corona. They do not find the same inconsistency between their measured $\tau_{\rm es}$ and radially uniform accretion that we found in Equation (6). This is a consequence of their $\dot{M}$ being higher and their $\tau_{\rm es}$ being lower than in our Cen X-4 observation. However, we noted in Section 4.1 that $\tau_{\rm es}$ and kT_e vary inversely, and the high kT_e values (and corresponding cutoff energies) that Sakurai et al. (2014) fit lie above their observation bandpass. The *Suzaku* data are thus unable to rule out the presence of a cutoff below 50–100 keV (but still above their bandpass); this would introduce the same difficulties for a Comptonization model that we found in Cen X-4, although it would be somewhat mitigated by the higher $\dot{M}$. We note that our bremsstrahlung model could explain the hard component in Aql X-1 for $kT_e \gtrsim 30$ keV.

It is interesting to also compare the behavior of Cen X-4 with systems that have been observed to transition between LMXB and radio pulsar states during X-ray quiescence. The theoretical expectation is that such transitions are controlled by the location of the NS magnetospheric boundary (Stella et al. 1994). We can compare r_m to both $r_{\rm co}$ and the light-cylinder radius:

$$r_{\rm lc} = \frac{cP}{2\pi} = 144\, P_{3\,\rm ms}\, \text{km}\,. \tag{56}$$

For sufficiently low $\dot{M}$, we have $r_{\rm co} < r_m < r_{\rm lc}$, and the system will be in the propeller regime, with accretion onto the NS (mostly) shut off (Illarionov & Sunyaev 1975; Ustyugova et al. 2006). For even lower $\dot{M}$, we will have $r_{\rm co} < r_{\rm lc} < r_m$. In this case, the radio pulsar mechanism can turn on, with the radiation pressure of a radio pulsar wind clearing the magnetosphere and an intrabinary shock giving rise to synchrotron X-ray emission (Stella et al. 1994; Campana et al. 1998a; Burderi et al. 2001). The $\dot{M}$ implied for transition to a millisecond radio pulsar state corresponds to $L_x \lesssim 10^{33}$ erg s, where the exact value depends on details of the system and the disk–magnetosphere interaction.

Indirect evidence for such transitions in NS/LMXBs during X-ray quiescence was previously reported in Aql X-1 ($L_x = 6 \times 10^{32}$ erg s^{-1}; Campana et al. 1998b) and SAX J1808.4−3658 ($L_x = 5 \times 10^{31}$ Burderi et al. 2003; Campana et al. 2004a; Deloye et al. 2008). However, more direct evidence has been reported more recently in at least three systems. The 1.7 ms radio pulsar PSR J1023+0038 (hereafter J1023) has made two transitions between the LMXB and radio pulsar states. It is now understood to have been in an LMXB state during 2000–2001, with direct optical evidence for the presence of an accretion disk (Wang et al. 2009). However, a state transition then occurred, with subsequent observations establishing the absence of an accretion disk during 2002–2013 (Thorstensen & Armstrong 2005) as well as the presence of a millisecond eclipsing radio pulsar during 2007–2013 (Archibald et al. 2009), along with a low X-ray luminosity associated with intrabinary synchrotron shock emission (Archibald et al. 2010; Bogdanov et al. 2011). A second state transition was observed more recently, with the radio pulsar turning off and an accretion disk reemerging (Stappers et al. 2014; Patruno et al. 2014).

In all of these observations, J1023 has remained in X-ray quiescence in the sense that a high-luminosity ($L_x \gtrsim 10^{36}$ erg s^{-1}) transient X-ray outburst was not observed. However, two distinct substates are evident: a faint X-ray–quiescent state ($L_x \sim 10^{32}$ erg s^{-1}) during which radio pulsations are seen, and a bright X-ray–quiescent state ($L_x \sim 10^{33}$ erg s^{-1}) during which the

radio pulsar is off. This suggests that r_m has moved outside the light cylinder in the fainter state. In both substates, the 0.3–10 keV X-ray emission has a power-law spectrum with little or no thermal component, with $\Gamma = 1.3$ in the faint state (Archibald et al. 2010) and $\Gamma = 1.69$ in the bright state (Patruno et al. 2014). *NuSTAR* observations show that these power-law spectra remain unbroken up to at least 79 keV (Tendulkar et al. 2014). During faint X-ray quiescence, the X-ray flux shows high-amplitude modulation at the orbital period (Archibald et al. 2010; Tendulkar et al. 2014), similar to what is seen in the X-ray emission from some (but not all) eclipsing millisecond radio pulsars (the so-called "black widow" and "redback" systems; Roberts 2013; Roberts et al. 2014). During bright X-ray quiescence, the X-ray flux shows strong, rapid flickering, with the intensity varying by an order of magnitude on timescales of <100 s (Patruno et al. 2014; Tendulkar et al. 2014).

A second object in which two LMXB/radio pulsar state transitions were seen is the M28 globular cluster source PSR J1824−2452I (hereafter M28I), a 3.9 ms radio pulsar. This radio pulsar underwent a bright transient X-ray outburst ($L_x \sim 10^{36}$ erg s^{-1}) in 2013 March, during which accretion-powered millisecond pulsations and a thermonuclear X-ray burst were observed, establishing the system as an NS/LMXB. The system returned to X-ray quiescence within a month, at which point radio pulsations were again detected (Papitto et al. 2013). These observations demonstrate that LMXB/radio pulsar state transitions can occur on timescales as short as days. During X-ray quiescence, rapid ($\lesssim$500 s) intensity variations of nearly an order of magnitude are again seen [$(0.6–4) \times 10^{33}$ erg s^{-1}], with no change in the 0.3–10 keV X-ray spectrum: an absorbed power law with $\Gamma = 1.2$ and no detectable thermal component (Linares et al. 2014). Remarkably, this rapid variability seems to toggle between two stable flux levels; Linares et al. (2014) suggest that this represents fast transitions between synchrotron shock emission and magnetospheric accretion. No orbital variability of the X-ray flux is reported in M28I.

The third object in which an LMXB/radio pulsar transition was seen is XSS J12270−4859 (hereafter J12270), a faint hard X-ray source associated with a relatively bright *Fermi* γ-ray source. During 2003–2012, the source was in a quiescent LMXB state with an absorbed power-law X-ray spectrum with $\Gamma = 1.7$, no evidence for a thermal spectral component, a 0.1–10 keV luminosity of $L_x = 2 \times 10^{33}\, D_{\rm kpc}$ erg s^{-1}, highly variable X-ray flaring, and multiwavelength evidence for the presence of an accretion disk (de Martino et al. 2010, 2013). In late 2012, the source made a transition to a lower ($6 \times 10^{31}\, D_{\rm kpc}$ erg s^{-1}) luminosity state with a power-law X-ray spectrum with $\Gamma = 1.2$, a thermal fraction $<9\%$, and a large-amplitude orbital modulation of the X-ray flux (Bassa et al. 2014; Bogdanov et al. 2014). After this transition, 1.69 ms radio pulsations were also detected (Roy et al. 2014).

Cen X-4 has a luminosity comparable to J1023, M28I, and J12270, and so it is presumably at least close to the regime where LMXB/radio transitions could occur. The rapid X-ray variability we observe (see Section 3.1) is quite different from the large-amplitude orbital modulation seen in the low-quiescent state of J1023, but it is qualitatively similar to (although somewhat weaker than) the flickering seen in the high-quiescent states of J1023 and J12270 as well as the M28I quiescent variability. On the other hand, unlike those three sources, the X-ray spectrum of Cen X-4 has a substantial thermal fraction ($\simeq$60%). This may indicate that more of the accretion flow reaches the surface of Cen X-4 than in the other systems. If we apply our Cen X-4 Compton-cooled bremsstrahlung model to the hard X-ray emission in J1023, M28I, and J12270 during their radio quiet or X-ray quiescent states, then we would expect a high (50–100 keV) electron temperature and an unbroken 2–10 keV power-law X-ray spectrum, consistent with what was observed.

Of course, synchrotron shock emission can also produce an unbroken power law in the X-ray band, and we expect this mechanism to dominate in the radio pulsar state. At sufficiently low luminosity, Cen X-4 should transition into a radio pulsar state; we suggest that this may be what occurs at $L_{\rm th} \lesssim 10^{32}\, D_{\rm kpc}^2$ erg s^{-1} in Figure 8 and that the jump in Γ might reflect a sharp transition from high-temperature bremsstrahlung emission to synchrotron shock emission. This is consistent with the suggestion by Jonker et al. (2004) that the power-law component in quiescent NS/LMXBs arises from accretion at higher $\dot{M}$ and from some different, nonaccretion mechanism (e.g., synchrotron shock emission) at lower $\dot{M}$; they used this to explain how the fractional power-law contribution to the quiescent luminosity varies with $\dot{M}$ in quiescent NS/LMXBs. It would be interesting to search for millisecond radio pulsations from Cen X-4 when its X-ray luminosity next drops to $\lesssim 10^{32}\, D_{\rm kpc}$ erg s^{-1}.

We thank the referee, Craig Heinke, for several suggestions that greatly improved our paper. D.C. thanks Herman Marshall, Sera Markoff, Caroline D'Angelo, Stephen Reynolds, Federico Bernardini, Phil Charles, and Chris Done for useful discussions and Luca Zampieri and Roberto Soria for sharing their XSPEC additive table model `zamp`. We also thank Thorsten Brand for help with evaluating the level of photon pileup in the *XMM-Newton* data. This work was supported in part under NASA contract NNG08FD60C and made use of data from the *NuSTAR* mission, a project led by the California Institute of Technology, managed by the Jet Propulsion Laboratory, and funded by NASA. We thank the *NuSTAR* Operations, Software, and Calibration teams for support with the execution and analysis of these observations. This research has made use of the *NuSTAR* Data Analysis Software (NuSTARDAS), jointly developed by the ASI Science Data Center (ASDC, Italy) and the California Institute of Technology (USA). J.A.T. acknowledges partial support from the *XMM-Newton* Guest Observer program through NASA grant NNX13AB47G.

Facilities: NuSTAR, *XMM*

REFERENCES

Archibald, A. M., Kaspi, V. M., Bogdanov, S., et al. 2010, ApJ, 722, 88
Archibald, A. M., Stairs, I. H., Ransom, S. M., et al. 2009, Sci, 324, 1411
Arnaud, K. A. 1996, in ASP Conf. Ser. 101, Astronomical Data Analysis Software and Systems V, ed. G. H. Jacoby & J. Barnes (San Francisco, CA: ASP), 17
Arons, J. 2002, in ASP Conf. Ser. 271, Neutron Stars in Supernova Remnants, ed. P. O. Slane & B. M. Gaensler (San Francisco, CA: ASP), 71
Arons, J., & Tavani, M. 1993, ApJ, 403, 249 (AT93)
Asai, K., Dotani, T., Hoshi, R., et al. 1998, PASJ, 50, 611
Bassa, C. G., Patruno, A., Hessels, J. W. T., et al. 2014, MNRAS, 441, 1825
Belian, R. D., Conner, J. P., & Evans, W. D. 1972, ApJL, 171, L87
Bernardini, F., Cackett, E. M., Brown, E. F., et al. 2013, MNRAS, 436, 2465
Bildsten, L., & Rutledge, R. E. 2000, ApJ, 541, 908
Blair, W. P., Raymond, J. C., Dupree, A. K., et al. 1984, ApJ, 278, 270
Blandford, R. D., & Begelman, M. C. 1999, MNRAS, 303, L1
Bogdanov, S., Archibald, A. M., Hessels, J. W. T., et al. 2011, ApJ, 742, 97
Bogdanov, S., Patruno, A., Archibald, A. M., et al. 2014, ApJ, 789, 40
Brown, E. F., Bildsten, L., & Rutledge, R. E. 1998, ApJL, 504, L95
Burderi, L., Di Salvo, T., D'Antona, F., et al. 2003, A&A, 404, L43

Burderi, L., Possenti, A., D'Antona, F., et al. 2001, ApJL, 560, L71
Cackett, E. M., Brown, E. F., Degenaar, N., et al. 2013, MNRAS, 433, 1362
Cackett, E. M., Brown, E. F., Miller, J. M., & Wijnands, R. 2010, ApJ, 720, 1325
Cackett, E. M., Fridriksson, J. K., Homan, J., et al. 2011, MNRAS, 414, 3006
Cackett, E. M., Wijnands, R., Heinke, C. O., et al. 2005, ApJ, 620, 922
Campana, S., Colpi, M., Mereghetti, S., Stella, L., & Tavani, M. 1998a, A&ARv, 8, 279
Campana, S., D'Avanzo, P., Casares, J., et al. 2004a, ApJL, 614, L49
Campana, S., Israel, G. L., Stella, L., Gastaldello, F., & Mereghetti, S. 2004b, ApJ, 601, 474
Campana, S., & Stella, L. 2003, ApJ, 597, 474
Campana, S., Stella, L., Mereghetti, S., et al. 1998b, ApJL, 499, L65
Canizares, C. R., McClintock, J. E., & Grindlay, J. E. 1980, ApJL, 236, L55
Chevalier, C., Ilovaisky, S. A., van Paradijs, J., Pedersen, H., & van der Klis, M. 1989, A&A, 210, 114
Conner, J. P., Evans, W. D., & Belian, R. D. 1969, ApJL, 157, L157
Coti Zelati, F., Campana, S., D'Avanzo, P., & Melandri, A. 2014, MNRAS, 438, 2634
D'Angelo, C. R., & Spruit, H. C. 2010, MNRAS, 406, 1208
D'Angelo, C. R., & Spruit, H. C. 2012, MNRAS, 420, 416
D'Avanzo, P., Campana, S., Casares, J., et al. 2005, A&A, 444, 905
Deloye, C. J., Heinke, C. O., Taam, R. E., & Jonker, P. G. 2008, MNRAS, 391, 1619
de Martino, D., Belloni, T., Falanga, M., et al. 2013, A&A, 550, A89
de Martino, D., Falanga, M., Bonnet-Bidaud, J.-M., et al. 2010, A&A, 515, A25
Deufel, B., Dullemond, C. P., & Spruit, H. C. 2001, A&A, 377, 955
Dickey, J. M., & Lockman, F. J. 1990, ARA&A, 28, 215
Evans, W. D., Belian, R. D., & Conner, J. P. 1970, ApJL, 159, L57
Frank, J., King, A., & Raine, D. 2002, Accretion Power in Astrophysics (3rd ed.; Cambridge: Cambridge Univ. Press)
Gaensler, B. M., & Slane, P. O. 2006, ARA&A, 44, 17
Guillot, S., Servillat, M., Webb, N. A., & Rutledge, R. E. 2013, ApJ, 772, 7
Harrison, F. A., Craig, W. W., Christensen, F. E., et al. 2013, ApJ, 770, 103
Heinke, C. O., Rybicki, G. B., Narayan, R., & Grindlay, J. E. 2006, ApJ, 644, 1090
Hjellming, R. M. 1979, IAUC, 3369, 1
Hjellming, R. M., Calovini, T. A., Han, X. H., et al. 1988, ApJL, 335, L75
Hua, X.-M., & Titarchuk, L. 1995, ApJ, 449, 188
Illarionov, A. F., & Sunyaev, R. A. 1975, A&A, 39, 185
Jansen, F., Lumb, D., Altieri, B., et al. 2001, A&A, 365, L1
Jonker, P. G., Galloway, D. K., McClintock, J. E., et al. 2004, MNRAS, 354, 666
Joss, P. C., & Li, F. K. 1980, ApJ, 238, 287
Kalberla, P. M., Burton, W. B., Hartmann, D., et al. 2005, A&A, 440, 775
Kaluzienski, L. J., Holt, S. S., & Swank, J. H. 1980, ApJ, 241, 779
Kennel, C. F., & Coroniti, F. V. 1984a, ApJ, 283, 694
Kennel, C. F., & Coroniti, F. V. 1984b, ApJ, 283, 710
King, A. R., Kolb, U., & Burderi, L. 1996, ApJL, 464, L127
Kulkarni, S. R., & Hester, J. J. 1988, Natur, 335, 801
Kuulkers, E., in't Zand, J. J. M., & Lasota, J.-P. 2009, A&A, 503, 889
Lasota, J.-P. 2001, NewAR, 45, 449
Lii, P. S., Romanova, M. M., Ustyugova, G. V., et al. 2014, MNRAS, 441, 86
Linares, M., Bahramian, A., Heinke, C., et al. 2014, MNRAS, 438, 251
Mahadevan, R., & Quataert, E. 1997, ApJ, 490, 605
Matsuoka, M., Inoue, H., Koyama, K., et al. 1980, ApJL, 240, L137
McClintock, J. E., & Remillard, R. A. 2000, ApJ, 531, 956
Menou, K., Esin, A. A., Narayan, R., et al. 1999, ApJ, 520, 276
Menou, K., & McClintock, J. E. 2001, ApJ, 557, 304
Narayan, R., Mahadevan, R., & Quataert, E. 1998, in The Theory of Black Hole Accretion Disks, ed. M. A. Abramowicz, G. Bjornsson, & J. E. Pringle (Cambridge: Cambridge Univ. Press), 148
Narayan, R., & Yi, I. 1995, ApJ, 452, 710
Papitto, A., Ferrigno, C., Bozzo, E., et al. 2013, Natur, 501, 517
Park, S., & Garcia, M. R. 2011, BAAS, 43, 144.25
Patruno, A., Archibald, A. M., Hessels, J. W. T., et al. 2014, ApJL, 781, L3
Psaltis, D., & Chakrabarty, D. 1999, ApJ, 521, 332
Roberts, M. S. E. 2013, in IAU Symp. 291, Neutron Stars and Pulsars: Challenges and Opportunities after 80 Years, ed. J. van Leeuwen (Cambridge: Cambridge University Press), 127
Roberts, M. S. E., McLaughlin, M. A., Gentile, P., et al. 2014, AN, 335, 313
Roy, J., Bhattacharyya, B., & Ray, P. S. 2014, ATel, 5890
Rutledge, R. E., Bildsten, L., Brown, E. F., Pavlov, G. G., & Zavlin, V. E. 1999, ApJ, 514, 945
Rutledge, R. E., Bildsten, L., Brown, E. F., Pavlov, G. G., & Zavlin, V. E. 2002, ApJ, 577, 346
Rybicki, G. R., & Lightman, A. P. 1979, Radiative Processes in Astrophysics (New York: Wiley)
Sakurai, S., Torii, S., Noda, H., et al. 2014, PASJ, 66, 10
Schlafly, E. F., & Finkbeiner, D. P. 2011, ApJ, 737, 103
Shahbaz, T., Watson, C. A., & Dhillon, V. S. 2014, MNRAS, 440, 594
Soria, R., Zampieri, L., Zane, S., & Wu, K. 2011, MNRAS, 410, 1886
Spruit, H. C., & Taam, R. E. 1993, ApJ, 402, 593
Stappers, B. W., Archibald, A. M., Hessels, J. W. T., et al. 2014, ApJ, 790, 39
Stappers, B. W., Gaensler, B. M., Kaspi, V. M., et al. 2003, Sci, 299, 1372
Stella, L., Campana, S., Colpi, M., Mereghetti, S., & Tavani, M. 1994, ApJL, 423, L47
Strüder, L., Briel, U., Dennerl, K., et al. 2001, A&A, 365, L18
Tendulkar, S. P., Yang, C., An, H., et al. 2014, ApJ, 791, 77
Thorstensen, J. R., & Armstrong, E. 2005, AJ, 130, 759
Titarchuk, L. 1994, ApJ, 434, 313
Titarchuk, L., & Lyubarskij 1995, ApJ, 450, 876
Torres, M. A. P., Casares, J., Martinez-Pais, I. G., & Charles, P. A. 2002, MNRAS, 334, 233
Turner, M. J. L., Abbey, A., Arnaud, M., et al. 2001, A&A, 365, L27
Ustyugova, G. V., Koldoba, A. V., Romanova, M. M., et al. 2006, ApJ, 646, 304
van Paradijs, J. 1996, ApJL, 464, L139
Vaughan, S., Edelson, R., Warwick, R. S., & Uttley, P. 2003, MNRAS, 345, 1271
Verner, D. A., Ferland, G. J., Korista, K. T., & Yakovlev, D. G. 1996, ApJ, 465, 487
Wang, Z., Archibald, A. M., Thorstensen, J. R., et al. 2009, ApJ, 703, 2017
Wijnands, R., Degenaar, N., & Page, D. 2013, MNRAS, 432, 2366
Wik, D. R., Hornstrup, A., Molendi, S., et al. 2014, ApJ, 792, 48
Wilms, J., Allen, A., & McCray, R. 2000, ApJ, 542, 914
Zampieri, L., Campana, S., Turolla, R., et al. 2001, A&A, 378, L5
Zampieri, L., Turolla, R., Zane, S., & Treves, A. 1995, ApJ, 439, 849